Multi-Material Topology Optimization of Structures with Discontinuities using Peridynamics

by

Anahita Habibian

A thesis Submitted in Partial Fulfillment of the
Requirements for the Degree of

MASTER OF APPLIED SCIENCE

in the Department of Mechanical Engineering

Multi-Material Topology Optimization of Structures with Discontinuities using Peridynamics

by

Anahita Habibian

Supervisory Committee

Dr. A. Suleman, Co-Supervisor
(Department of Mechanical Engineering)

Dr. B. Nadler, Co-Supervisor
(Department of Mechanical Engineering)

ABSTRACT

This study proposes an approach for solving density-based multi-material topology optimization of cracked structures using Peridynamics. The alternating active-phase algorithm is utilized to transform the multi-material problem into a series of binary phase topology optimization sub-problems. Instead of the conventional mesh-based methods, the Peridynamics theory (PD) is used as a tool to model the behaviour of the materials and solve for the displacement field. The most significant advantage of PD is its ability to model discontinuities in a relatively straightforward manner. Thus, in the present work, the effect of cracks as a discontinuity is investigated on the optimal multi-material topologies. The Solid Isotropic Material with Penalty (SIMP) method is utilized to define the material properties as a function of the design variables. Also, the optimization problem is solved through the Optimality Criteria (OC) approach. The proposed method is compared to the results reported in the literature by executing three numerical examples that investigate the effect of the direction of an interior crack on the optimal topologies. Moreover, the efficiency of the proposed approach is verified by solving several examples where we aim at minimizing the compliance of the structure with and without initial cracks.

Table of Contents

Supervisory Committee **ii**

Abstract **iii**

Table of Contents **iv**

List of Tables **vi**

List of Figures **vii**

Acknowledgements **ix**

Dedication **x**

1 Introduction **1**

1.1 Topology optimization methods 1

1.1.1 Homogenization method 1

1.1.2 SIMP method 2

1.1.3 ESO and BESO methods 3

1.1.4 Level-set method 5

1.1.5 Phase-field method 6

1.1.6 Alternating active-phase algorithm 7

1.2 Meshless methods 8

1.3 Topology optimization of cracked structures 9

1.4 Peridynamics 10

1.5 Novelty 12

1.6 Agenda 13

2 Peridynamics theory **14**

2.1 Deformation 15

2.2 Force density 16
2.3 Strain energy density 16
2.4 Equation of motion 17
2.5 Boundary conditions 18
2.6 Balance laws 18
2.7 Bond-based Peridynamics 20
2.7.1 Bond-based Peridynamics for isotropic materials in 2D analysis 22
2.8 Cracks 26
2.9 Numerical solution method 26
2.9.1 Spatial integration 27
2.9.2 Time integration 27

3 Topology Optimization **31**
3.1 Alternating Active-Phase Algorithm 32
3.1.1 Modification of PD bond constant for the application of multi-material structures 35
3.2 Optimality Criteria Method 37
3.3 Filtering 38

4 Examples and Discussions **40**
4.0.1 The effect of the direction of interior cracks 41
4.0.2 Example 1: Cantilever Beam 42
4.0.3 Example 2: L-Shape Structure 44
4.0.4 Example 3: Bridge with Uniform Pressure Load 46
4.0.5 Example 4: Bridge 47

5 Conclusions and future work **69**

Appendix A Balance of linear and angular momentum **71**

Bibliography **73**

List of Tables

Table 4.1 Material properties of each material 48

List of Figures

Figure 1.1 The application of TO in aerospace industry: A 20% decrease in the mass of the leading edge rib of Airbus A380 by using TO . 2
Figure 1.2 Comparison of MD, CCM, and PD 11

Figure 2.1 family of the material point i 15
Figure 2.2 Undeformed and deformed states of the body 15
Figure 2.3 Deformation of material points $\mathbf{x}$ and $\mathbf{x}'$ in bond-based formulatio 20
Figure 2.4 Deformation of material points $\mathbf{x}$ and $\mathbf{x}'$ in state-based formulation 20
Figure 2.5 A schematic of a 2D plate deformation under simple shear . . . 25
Figure 2.6 Broken PD bonds (in red) due to the existence of a crack . . . 26

Figure 3.1 flowchart of an alternating active-phase algorithm 36

Figure 4.1 Studying the effect of the direction of the interior crack 41
Figure 4.2 Comparison of optimal solutions (left column: PD-TO results, right column: X-FEM results) 43
Figure 4.3 Strain energy density (left column) and total displacement (right column) distribution of the horizontal, vertical, and inclined interior cracks 44
Figure 4.4 Displacement distribution of the horizontal, vertical, and inclined interior cracks in x (left column) and y directions (right column) 45
Figure 4.5 Design domain of the cantilever beam 46
Figure 4.6 Optimal design of the cantilever beam with no initial cracks . . 46
Figure 4.7 Optimal design of the cantilever beam with an initially embedded crack 47
Figure 4.8 Strain energy density distribution of the cantilever beam 47
Figure 4.9 Displacement distribution of the cantilever beam in x-direction 48
Figure 4.10Displacement distribution of the cantilever beam in y-direction 49
Figure 4.11Total displacement distribution of the cantilever beam 50

Figure 4.12Design domain of the L-Shape structure 50
Figure 4.13Optimal topology of the L-shape beam with no cracks 51
Figure 4.14Optimal topology of the L-shape beam with an embedded crack at the knee 51
Figure 4.15Strain energy density distribution of the L-Shape structure . . . 52
Figure 4.16Displacement distribution of the L-Shape structure in x-direction 53
Figure 4.17Displacement distribution of the L-Shape structure in y-direction 54
Figure 4.18Total displacement distribution of the L-Shape structure 55
Figure 4.19Design domain of the bridge with uniform pressure load 55
Figure 4.20Optimal topology of the bridge under uniform pressure without initial crack 56
Figure 4.21Optimal topology of the bridge under uniform pressure with an initially embedded crack 56
Figure 4.22Strain energy density distribution of the bridge under uniform pressure 56
Figure 4.23Displacement distribution of the bridge under uniform pressure in x-direction 57
Figure 4.24Displacement distribution of the bridge under uniform pressure in y-direction 58
Figure 4.25Total displacement distribution of the bridge under uniform pressure 59
Figure 4.26Design domain of the bridge with two interior cracks 59
Figure 4.27Optimal result of the three-material bridge structure 60
Figure 4.28Optimal result of the four-material bridge structure 60
Figure 4.29Optimal result of the three-material cracked bridge structure . . 60
Figure 4.30Optimal result of the four-material cracked bridge structure . . 60
Figure 4.31Strain energy density distribution of the three-material bridge . 61
Figure 4.32Displacement distribution of the three-material bridge in x-direction 62
Figure 4.33Displacement distribution of the three-material bridge in y-direction 63
Figure 4.34Total displacement distribution of the three-material bridge . . 64
Figure 4.35Strain energy density distribution of the four-material bridge . 65
Figure 4.36Displacement distribution of the four-material bridge in x-direction 66
Figure 4.37Displacement distribution of the four-material bridge in y-direction 67
Figure 4.38Total displacement distribution of the four-material bridge . . . 68

ACKNOWLEDGEMENTS

I would like to thank Dr. Afzal Suleman for allowing me to work with him, and appreciate all the continued support I received throughout this project. I would also like to thank Dr. Ben Nadler for his advice.

My special thanks to Dr. Abdolrasoul Sohouli for his consistent guidance, thoughtful comments and recommendations. I would not have been able to complete this research without him.

To the committee members, I want to express my gratitude for their time and effort to evaluate my work.

Finally, I would like to thank my colleagues in the CfAR computational group, many of whom I can nowadays call friends. I'm thankful for the friendly environment they provided and their unconditional support.

DEDICATION

I dedicate my work to my loving parents.

Chapter 1

Introduction

The well-known topology optimization problem (TO) has attracted attention, particularly from aerospace and automotive industries, since it was first introduced by [Bendsøe and Kikuchi(1988)]. The structural topology optimization problem deals with finding the mass/material distribution over a predefined spatial design domain by optimizing an objective function subjected to relevant constraints. Since the structures designed from an engineering perspective are usually conservative for safety reasons, they contain excessive material. To remove such excessive material, TO techniques can be readily employed. However, TO problem is inherently ill-posed, which leads to numerical instabilities, such as checkerboard patterns and mesh dependency issues. This ill-posed problem was initially solved by the introduction of the homogenization method [Bendsøe and Kikuchi(1988)], which discretizes the design domain into small elements and defines their relative densities as design variables. Since topology optimization was introduced in 1988, various methods have emerged to solve the problem. A list of the common approaches in this filed are provided in the following sections along with a concise overview of each them and their applications.

1.1 Topology optimization methods

1.1.1 Homogenization method

The first method proposed to resolve the ill-posed problem was the homogenization method [Bendsøe and Kikuchi(1988)]. In this approach, the design domain is discretized into small elements, and the relative densities of those elements are considered as design variables. This was proposed to relax the "0-1" problem, which stems from the

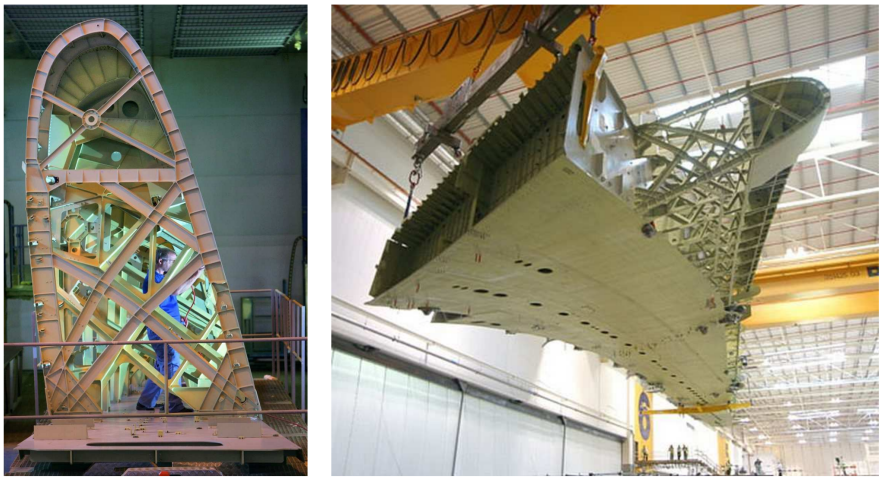

Figure 1.1: The application of TO in aerospace industry: A 20% decrease in the mass of the leading edge rib of Airbus A380 by using TO

fact that the mass distribution is represented by an artificial relative density ranging from 0 to 1 (0 for voids and 1 for solid parts). A question arises as to whether such a material structure physically exists, especially if intermediate gray-scale areas remain in the final topology. However, this is not a concern in the homogenization method, since it is based on the microstructure variation of a composite material consisting of a material and an oriented void [Yin and Ananthasuresh(2001)]. Moreover, this approach can make internal holes into the structure without knowing their existence in advance. Therefore, it can be used to perform shape and topology optimization simultaneously.

1.1.2 SIMP method

Later, SIMP was introduced by [Bendsøe(1989), Zhou and Rozvany(1991)]. This method originates from the homogenization approach and the design variables are the artificial relative densities of the elements. In addition, the material properties of the elements (e.g., elastic modulus) are expressed through an interpolation power function along with a penalization factor. One significant advantage of the SIMP is that it can readily be extended to include multiple materials. The SIMP method has recently become popular for topology optimization problems as a result of its conceptual simplicity, easy-to-implement nature and computational efficiency. For instance, [Yin and Ananthasuresh(2001)] used a gradually formed continuous peak function for material

interpolation and the optimality criteria (OC) to synthesize multi-material compliant structures. Their numerical examples include two/three/four-phase materials where void is treated as one phase. Moreover, [Zuo and Saitou(2017)] proposed the ordered multi-material SIMP interpolation to express the material properties of the elements. Also, a combination of mass and cost constraint is considered in their work to solve the compliance minimization problem using a heuristic updating scheme of the design variables from the Kuhn-Tucker (KKT) optimality condition. Another contribution to multi-material TO was made by [Sigmund(2001)] ,where the SIMP method is used to design multi-physics actuators with the particular application of designing thermally and electrothermally driven microactuators to use in MicroElectroMechanical Systems (MEMS). Additionally, [Luo and Kang(2013)] state the topology optimization problem of reinforced concrete structures as a minimum compliance problem under the yield stress and volume constraints. Recently, [Blasques(2014)] has presented a SIMP-like method for simultaneous cross-section topology and material optimization of laminated composite beams under Eigen frequency constrains.

1.1.3 ESO and BESO methods

In 1993, Xie and Steven introduced a bio-inspired method referred to as evolutionary structural optimization (ESO) to the existing state-of-the-art for TO [Xie and Steven(1993)]. The inspiration for the ESO method stems from the evolution of naturally occurring structures such as bones and trees. By observing this evolution, it becomes evident that the structure's topology and shape evolve over a long period to adapt to its environment. It is shown that the same logic can be applied to engineering structural design problems through FEM. During optimization, the ESO algorithm removes the excessive material iteratively until a set of predefined volume constraints are satisfied. The first proposed ESO procedure consists of deleting the elements the von Misses stress of which is less than threshold, which is the rejection ration (RR) times the maximum von Misses stress over the whole structure. Next, a finite element analysis is repeated to determine the new state of stress until a steady-state is achieved.Afterwards, an evolution rate (ER) is introduced and added to the current RR to increase the RR for the next iteration. Another iteration takes place until the steady-state is reached, meaning that the result is a fully stressed design where all the members support the same maximum stress. This approach provides the possibility of knowing every step of the evolution process towards the optimum solution. A

remarkable benefit of the ESO method is that there is no need to generate e new mesh at each stage of the evolution; instead, the properties of the rejected elements are assigned to zero. It is worth mentioning that the evolution rate ER should not be too high, otherwise, over rejection happens, and the structure becomes singular. A commonly asked question about the accuracy of the ESO method is whether the method can guarantee that the optimal solution achieved is not a local optimum, and if the elements once removed can be returned. Later,bi-directional ESO (BESO) was proposed by [Querin et al.(2000b)Querin, Young, Steven, and Xie] to search for all possible directions, including not only material removal but the addition of material to elements with high-stress levels. The BESO approach evolved from ESO and additive evolutionary structural optimization (AESO) [Querin et al.(2000a)Querin, Steven, and Xie] methods. In AESO, the structure expands from a basis, which is the minimum structural form connecting the domain between the loads and supports regardless of the magnitude of the stress levels. Then, material is added to areas with high stress. However, the final solution can be over-designed because the initial design domain can never be removed. Thus, the BESO method is a combination of ESO and AESO methods using which the designer can choose between an initial design domain fitting the maximum allowable area or the least number of elements as in the AESO approach. In addition, the ESO method requires that the structural modifications be kept minimal per cycle, which makes it very costly in terms of computational expenses [Eschenauer and Olhoff(2001)]. On the contrary, the BESO approach is more efficient in terms of computational costs and time, since the initial physical structure can contain a minimal number of elements. However, both ESO and BESO methods are a combination of an entirely intuitive-heuristic and a gradient-based approach [Eschenauer and Olhoff(2001)]. In BESO, elements can be removed from regions that are heavily under-stressed and can be added to heavily over-stressed areas. Many works have been dedicated to the BESO method over the last two decades and solved various complex topology optimization problems. [Yang et al.(1999)Yang, Xie, Steven, and Querin] used the BESO method considering stiffness and displacement constraints for the problem. They studied the theoretical aspects of this method, such as the sensitivity number. Also, [Huang and Xie(2009)] proposed a new BESO method with a penalization parameter to design structures with one or multiple materials and showed that the optimal design is independent of the degree of penalization.

1.1.4 Level-set method

Another common approach in topology optimization is the Level-set method [Osher and Sethian(1988), Sethian and Wiegmann(2000)], which monitors the geometry changes of the boundaries by the motion of level sets. In other words, the boundaries of the structure are represented as zero level sets, using higher-order surfaces. Afterwards, by solving the Hamilton-Jacobi partial differential equations (PDEs), the topology changes can be tracked through the emerging and splitting of the boundaries. The advantage of the level-set is that the proposed models are flexible in terms of the topology changes since it's straightforward to form holes, splits and merge pieces. [Allaire et al.(2004)Allaire, Jouve, and Toader, Wang et al.(2003)Wang, Wang, and Guo] developed shape-sensitivity analysis for the level-set method. Because the current method offers an explicit mathematical expression, it facilitates the sensitivity analysis. One notable drawback of this approach is its slow convergence rate. Also, its final solution significantly depends on the initial design, thereby posing another shortcoming. Up to date, the level-set method has been utilized for various single material topology optimizations. For example, [Allaire and Jouve(2005)] extended the level-set approach to new objective functions such as Eigen frequencies and multiple loads. Moreover, [Allaire and Jouve(2008)] chose the objective function of the topology optimization problem to be stress minimization. Additionally, optimal geometry of functionally graded structures were determined using this approach [Xia and Wang(2008)]. Another application of the level-set method involves multi-material topology optimization problems. Generally, $m = log_2^n$ level-set functions are required for n material phases. Specifically, [Wang and Wang(2004)] generalized the level-set based approach using a multi-phase model proposed in [Vese and Chan(2002)] to solve the stress-related multi-material topology optimization. Later, [Wang et al.(2015)Wang, Luo, Kang, and Zhang] proposed a new Multi-Material Level Set (MM-LS) topology description for shape optimization of multi-material structures. The core idea of their method is to express the material properties by combining the level-set functions. The MM-LS model employs only M level-set functions for $M + 1$ phases. [Wang and Wang(2005)] adapted the Mumford-Shah model [Mumford and Shah(1989)] to propose a level-set based variational approach for design and optimization of heterogeneous objects. [Luo et al.(2009)Luo, Tong, Luo, Wei, and Wang] proposed the piecewise constant level-set method for shape and topology optimization of compliant multi-material mechanism with piezoelectric actuators to overcome the numerical difficulties related to solving

the Hamilton-Jacobi PDEs.

1.1.5 Phase-field method

As mentioned above, the level-set is a boundary variation approach. In addition to this method, phase-field method is a well-known approach where, unlike density-based methods, an implicit function is used to define structural boundaries rather than an explicit parameterization of the design domain. The idea of the phase-field method in topology optimization originates from surface dynamics simulations, especially in materials science, such as diffusion, solidification, and phase transition. Traditional phase-field models are developed based on Cahn-Hilliard [Cahn(1961), Cahn and Hilliard(1958), Cahn and Hilliard(1959)] and Cahn-Allen [Allen and Cahn(1979)] equations from metallurgy to represent phase segregation in binary alloy systems. In this method, a phase-field function is defined over the design domain consisting of two phases (solid or fluid) and the boundary region between these phases is a varying area of a thin finite thickness, which is modified via dynamic evolution equations of the phase-field function. The goal is to characterize the stability of this multi-phase system and describe the interface boundaries while the system is experiencing a physical process (e.g. diffusion) to achieve a steady-state. It is assumed that all material properties change smoothly over the design domain such that no jumps are resulting in singularities. The significant difference between level-set and phase-field methods is that in the phase-field method, the phase transition equations are solved without initial information about the location of the phase interface area, whereas in the level-set method, the boundary interface is monitored during optimization. Also, one advantage of the phase-field method over the level-set method is the fact that there is no need to reinitialize the step of level set functions. The problem of topological changes in phase transition is identical to the topology optimization problem. Therefore, [Bourdin and Chambolle(2003), Bourdin and Chambolle(2006)] took advantage of this similarity and employed the phase-field method in topology optimization for the first time. Later, [Burger and Stainko(2006)] solved the topology optimization problem with local stress constraints, using a phase-field method. They demonstrated the performance of this method on benchmark beam examples. [Takezawa et al.(2010)Takezawa, Nishiwaki, and Kitamura] developed a new intuitive phase-field method for topology optimization, using a time-dependent reaction-diffusion equation (Allen-Cahn equation). Their proposed approach is applied to three different problems: minimum compliance

problem, compliant mechanism design problem, and eigenfrequency maximization problem. The phase-field method is also used to solve three-dimensional topology optimization problems. [Dedè et al.(2012)Dedè, Borden, and Hughes] employed generalized Cahn-Hilliard equations to solve the minimum compliance case of TO. It is stated in their work that the mesh dependency effect can be reduced by choosing a suitable set of parameters controlling the thickness of the interfaces and the number of holes in the topology. Similar to other topology optimization methods, the phase-field method was used to find a solution to the multi-material topology optimization problem [Blank et al.(2014)Blank, Farshbaf-Shaker, Garcke, Rupprecht, and Styles, Wang and Zhou(2005)]. [Zhou and Wang(2007)] used the phase-field method along with a generalized Cahn-Hilliard model to minimize the mean compliance of a multi-material structure. They transform the structural topology optimization problem into a phase transition problem by considering the bulk energy and interface energy of the phases and the elastic strain energy of the structure. To demonstrate the performance of their method, some two and three-dimensional examples are studied. Recently, the phase-filed method was employed to vibrating structures to reduce dynamic performance variability [Zhang et al.(2019)Zhang, Takezawa, and Kang]. The objective function is a weighted summation of the mean value of the dynamic structural compliance, the fundamental frequency (frequency gap), and the transient displacement under impact loads, together forming the overall dynamic performance. They also take into account uncertain diffuse-region due to manufacturing-related errors.

1.1.6 Alternating active-phase algorithm

Recently, the alternating active-phase algorithm is introduced by [Tavakoli and Mohseni(2014)] to extend the topology optimization solvers from the traditional binary phase to multi-phase. In this approach, a multi-phase TO problem is sequentially split into a series of binary phase sub-problems. The benefits of the alternating active-phase algorithm are its simplicity, generality, and ease of implementation. However, it has some shortcomings such as its limited application due to the fact that it is a monotonic optimization solver and thus it cannot be used for non-monotonic problems. Later, [Majdi and Reza(2020)] used this algorithm to design three-phase compliant mechanisms, including a gripper, an inventor, and a cruncher. To validate the results, the maximum displacement of the compliant mechanisms is compared with the results obtained from a finite element based software.

1.2 Meshless methods

Most of the works mentioned above employed mesh-dependent methods. However, some issues limit the use of mesh-based numerical methods for topology optimization applications. For instance, when dealing with large deformation or moving boundaries, re-meshing the finite element model is inevitable. The major problems involved with large deformation when using element-based methods can be categorized into two groups. First, mesh distortion phenomena when the meshes become extremely skewed or compressed, which can worsen the numerical analysis of the displacement field. Secondly, the issue of local instability which might occur in areas with low densities. Consequently, most studies in the topology optimization field assume small deformations. Furthermore, introducing failure (e.g., cracks) to the structure is a mathematically complex procedure. To overcome these difficulties, topology optimization based on meshless methods has emerged. The meshless methods use some nodes scattered over the design domain and on the boundaries. These nodes do not serve as meshes; as a result, no information is needed on the relationships between the nodes to interpolate the unknown variables. The most common meshless methods in TO are as follows: smooth particle hydrodynamics (SPH) [Monaghan(2012)], element-free Galerkin (EFG) [Belytschko et al.(1994)Belytschko, Lu, and Gu], meshless local Petrov-Galerkin (MLPG) [Atluri and Zhu(1998)], reproducing Kernel particle method (RKPM) [Liu et al.(1995)Liu, Jun, and Zhang], collocation meshless method [Zhang et al.(2001)Zhang, Liu, Song, and Lu], and spline-based mesh-free method (SBMFM) [Hur et al.(2017)Hur, Kang, and Youn]. Recently, meshless methods have achieved significant progress. For example, [Luo et al.(2012)Luo, Zhang, Gao, and Ma] used the global weak form of the EFG method with compactly supported radial basis functions (CSRBFs) as an interpolation method to construct the shape functions. The CSRBF method originates from the radial basis function (RBFs) method, which is inherently meshless and provides interpolations with no need for a mesh grid and ensures an accurate interpolation. Nevertheless, they create poorly conditioned matrices, which causes numerical difficulties. On the other hand, CSRBFs can create strictly positive definite matrices to facilitate numerical performance. Moreover, the interpolant functions are continuous, so their derivatives are smooth. In their work, the original shape and topology optimization based on level-set equations, is transformed into an easier size optimization. [Cho and Kwak(2006)] used the reproducing kernel (RK) method for topology optimization of nonlinear structures

to discretize the displacement and density fields so that the points can be easily removed from or added to the design domain. As a result, the convergence problem of low-density areas can be avoided by excluding those sub-domains. Later, [Zheng et al.(2009)Zheng, Long, Xiong, and Li] solved the topology optimization problem by employing the finite volume meshless local Petrov-Galerkin (FVMLPG) and the moving least square (MLS) method for interpolation of strain and displacement. They chose a combination of SIMP and OC methods to minimize the compliance of the structure as the objective function. Using the EFG method to discretize the analysis domain and the independent Point-wise Density Interpolation [Kang and Wang(2011)], which is constructed by Shepard function, [He et al.(2014)He, Kang, and Wang] solved the topology optimization problem for geometrically nonlinear structures. All of the works above employed meshless methods for single-material topology optimization; however, [Cui et al.(2017)Cui, Chen, Zhou, and Wang] applied the EFG method to analyze multi-material structures, where a combination of Shepard interpolation and Moving Least Square (MLS) is chosen to build the shape functions. Usually, meshless methods are costlier than mesh-based approaches in terms of computations. Therefore, combining these two methods can significantly reduce the computational cost. Accordingly, [Zhang et al.(2018)Zhang, Ge, Zhang, and Zhao] coupled FEM and EFG method to reduce the computational cost. This method can guarantee the continuity of the shape function in the coupling areas. It has been found that the ESO (BESO) methods are mesh-dependent and to resolve this problem, [Juan et al.(2010)Juan, Shuyao, and Guangyao] applied the EFG method, combined with ESO to design a continuum structure by minimizing the structure weight. Also, [Zhao(2014)] utilized the BESO method with the EFG method as their meshless method and to construct the shape functions, they used the CSRBF interpolation approach.

1.3 Topology optimization of cracked structures

The presence of discontinuities, such as cracks, and hidden failures is a prevalent issue for most of the engineering structures. When the crack is not considered in the analysis, despite its existence, the optimal design cannot be reliable. Therefore, using topology optimization plays a vital role to achieve reinforced structures that can endure even with embedded cracks. However, up to date, only a few works are dedicated to this matter. To give an instance, [Shobeiri(2015)] used the EFG method along with BESO

to find the optimal design of a single-material structure with initially embedded cracks. They studied the effect of crack size and location on the final topology as well. Later, the idea of topology optimization of cracked structures was extended to multi-material cases. In this regard, [Banh and Lee(2018)] introduced a novel mesh-based numerical approach using the alternative active-phase algorithm. Moreover, they investigated the dependence of the designs on the size, location, orientation, and the number of initial cracks. Recently, [Xia et al.(2018)Xia, Da, and Yvonnet] utilized the BESO method to improve the fracture resistance (the required mechanical work for complete failure) of quasi-brittle composites through optimal placement of the inclusion phase. A finite element method is used for both displacement and crack phase fields.

1.4 Peridynamics

Peridynamics (PD) [Silling(2000), Silling et al.(2007)Silling, Epton, Weckner, Xu, and Askari, Silling and Askari(2005)] is a nonlocal theory that belongs to the class of continuum mechanics formulations. The behaviour of material due to different loading and boundary conditions can be studied at various length scales. At one end of this range, usually, Molecular Dynamics (MD) is used to analyze the interactions of atoms and molecules at the Nano-scale. However, this theory is costly in terms of computational expenses, which limits this method's practicality in engineering problems. At the other end, the behaviour of a body is often studied using the Classical Continuum Mechanics at the macro-scale. In Classical Continuum Mechanics (CCM), the governing equation of a continuum body is a partial differential equation containing spatial derivatives. Although when discontinuities such as cracks exist in the body, these well established equations face difficulties as a result of singular spatial derivatives. To tackle this problem, some approaches have been proposed, such as Linear Elastic Fracture Mechanics (LEFM) [Griffits(1995), Francfort and Marigo(1998)] and Cohesive Zone Model (CZM)[Barenblatt(1959), Dugdale(1960)]. In PD, a body is subdivided into material points taking volume in space. The behaviour of these material points is described through their nonlocal interactions with other material points in their neighbourhood. Unlike CCM formulation, PD uses integrodifferential equations instead of partial differential equations which do not contain any spatial derivatives. Consequently, PD is an attractive candidate for modelling problems including discontinuities, and the material does not necessarily require to remain continuous after deformation. Moreover, the non-locality present in

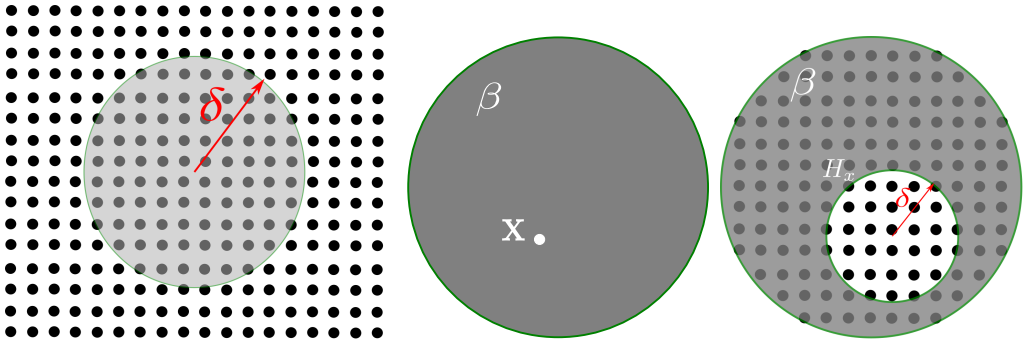

(a) Molecular dynamics (MD) (b) Classical continuum mechanics (CCM) (c) Peridynamics (PD)

Figure 1.2: Comparison of MD, CCM, and PD (regenerated from [Javili et al.(2019)Javili, Morasata, Oterkus, and Oterkus])

PD's equation of motion establishes a relation between CCM and MD; therefore, PD can be readily used in modelling different length scale structures. Figure 1.2 outlines the similarities and differences among MD, CCM, and PD schematically.

One of the most significant benefits of PD is its ability to predict damage with no need for an external damage law for crack initiation and propagation. Additionally, damage can naturally nucleate in an unspecified location and cracks can grow through unguided paths without any singularity. Furthermore, multiple damage sites and their complex interactions can emerge in the same area. Overall, PD does not require any simplifying assumptions to identify fracture modes as opposed to traditional continuum mechanics. Therefore, the PD method has been successfully used to simulate crack growth [Silling and Askari(2005)] and failure on multi-scale structures [Basoglu et al.(2019)Basoglu, Zerin, Kefal, and Oterkus], as well as damage prediction of different materials, such as composites [Hu et al.(2012)Hu, Ha, and Bobaru, AlKhateab et al.(2020)AlKhateab, Tabrizi, Zanjani, Rahimi, Poudeh, Kefal, and Yildiz] and layered heterogeneous materials [Jung and Seok(2016)]. PD also has proven to be a powerful tool to capture different types of fractures. For instance, [Silling(2003)] used PD to study dynamic fracture. Further studies were done to analyze the dynamic fracture of various types of structures, including concrete structures [Huang et al.(2015)Huang, Lu, and Liu], anisotropic [le Hu et al.(2014)le Hu, Yu, and Wang], functionally graded materials [Cheng et al.(2015)Cheng, Zhang, Wang, and Bobaru, Ozdemir et al.(2020)Ozdemir, Kefal, Imachi, Tanaka, and Oterkus], and quenched glass plates [Kilic and Madenci(2009)]. Moreover, it is shown that Peridynamic theory can be utilized to study fatigue. E.g., [Hu and Madenci(2017)] proposed a fatigue

model to predict damage in laminates under cyclic loading.

1.5 Novelty

Considering PD's ability to permit and predict discontinuities, PD-based topology optimization can provide a powerful platform to account for such imperfections so that structures can be improved at the conceptual design phase. The first attempt to merge PD with TO for cracked structures was made in [Kefal et al.(2019)Kefal, Sohouli, Oterkus, Yildiz, and Suleman], where the authors utilized the direct solution approach to solve PD equations at each optimization step. This innovative coupling was named as PD-TO, which yields in computationally efficient analysis for topology optimization of structures with initially embedded cracks. The PD-TO was first established based on the BESO approach. Recently, it was successfully extended to gradient-based topology optimization algorithms and extensively validated for complex engineering problems involving cracks [Sohouli et al.(2020)Sohouli, Kefal, Abdelhamid, Yildiz, and Suleman].

To the best of authors' knowledge, none of the above-mentioned works used PD-TO method to analyze multi-material structures with initially embedded cracks. The only study that investigated topology optimization of cracked multi-material structures is [Banh and Lee(2018)], which uses the X-FEM method. However, one of the drawbacks of X-FEM is its requirement for external criteria, such as virtual crack closure or maximum stress techniques to introduce cracks. Also, it needs other methods, e.g. level-set, to track crack propagation. In case of complex crack paths, where a crack is embedded in the element boundaries without cutting the edges, or in case of the presence of more than one crack in an element, the X-FEM approach poses various challenges when following complex crack paths. On the other hand, the nature of PD theory enables us to define cracks or defects within the structure in a straightforward manner, and no complicated mathematical expression is required to predict crack initiation, growth pattern and fracture modes. Moreover, PD theory can easily handle problems with moving boundaries and large deformations since there is no need to maintain mesh connectivity. As a result, using PD theory can be more beneficial for topology optimization of cracked structures as compared to X-FEM. Hence, the main novelty of this study is to introduce multi-material topology optimization of cracked structures based on PD-TO for the first time in the literature. It should be noted that multi-material designs are a class of composite structures.

1.6 Agenda

The present work includes five chapters and is structured as follows:

Chapter 1 contains a review of the topology optimization emergence and the various conventional methods introduced up to date to solve several TO problems. Besides, meshless approaches, their pros and cons, along with the applications in TO have been reviewed. Next, the importance and impact of initially embedded cracks into the structure, on topology optimization, and a summary of the studies regarding TO of cracked structures is provided. An overview of Peridynamics, its features and advantages is introduced afterwards. Lastly, the novelty, and the overall motivation for the current research has been stated, followed by an outline of the structure of the document itself.

Chapter 2 describes in details the Peridynamics theory, the derivation of PD's equation of motion, in conjunction with the modifications imposed by bond-based formulation, in case of a two-dimensional isotropic structure. Moreover, the numerical approach utilized to sole PD equations is introduced.

Chapter 3 presents the topology optimization problem with the objective of compliance minimization through the alternating active-phase algorithm. Next, the optimality criteria method is explained, followed by the description of filtering concept.

Chapter 4 includes the evaluation of the present method and compares with others' work in this area through three distinct case studies, together with investigation and examples for the proposed multi-material PD-TO approach.

Chapter 5 contains a restatement of the claims and the results of this dissertation.

Chapter 2

Peridynamics theory

The peridynamics theory is a nonlocal formulation of continuum mechanics. The term "*peridynamics*" comes from two Greek words, "*peri*", meaning around and "*dynami*", meaning force. To obtain the response of a solid structure subjected to external forces, the classical continuum mechanics assumes the structure as a continuous body, by ignoring its atomic structure. In continuum mechanics, the body consists of an infinite number of infinitesimal volumes called material points. These material points interact only with other ones located in their immediate vicinity. These interactions are expressed as forces or tractions, $\mathbf{T}$. By employing the conservation of linear and angular momentum and relating the traction forces to the stress tensor, $\boldsymbol{\sigma}$ as $\mathbf{T} = \boldsymbol{\sigma} \cdot \boldsymbol{n}$ where $\boldsymbol{n}$ is the unit normal of the surface the traction is acting on, the equation of motion of material point, $\boldsymbol{x}$, in classical continuum mechanics can be expressed as follows:

$$\rho(\boldsymbol{x})\ddot{\boldsymbol{u}}(\boldsymbol{x}, t) = \nabla \cdot \boldsymbol{\sigma} + \boldsymbol{b}(\boldsymbol{x}, t) \tag{2.1}$$

where $\rho(\boldsymbol{x})$, $\boldsymbol{b}(\boldsymbol{x}, t)$, and $\ddot{\boldsymbol{u}}(\boldsymbol{x}, t)$ represent the mass density, body force, and acceleration of the material point $\boldsymbol{x}$, respectively. The existance of the divergence operator in (2.1) makes this equation invalid for problems including discontinuities, such as cracks.

As opposed to CCM, in PD, the behavior of a material point is governed by its direct physical interactions (called *bond*) with all material points within its range. The range of particle $\boldsymbol{x}$ is denoted by $\delta > 0$, referred to as the *horizon*. Also, the material points within the distance δ of $\boldsymbol{x}$ are called the *family* of $\boldsymbol{x}$, H, as illustrated in Figure 2.1. Simply put, a material point can not see beyond its horizon.

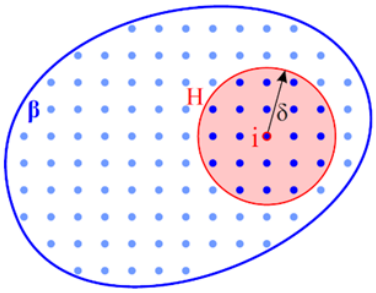

Figure 2.1: family of the material point i [Kefal et al.(2019)Kefal, Sohouli, Oterkus, Yildiz, and Suleman]

2.1 Deformation

In the undeformed state of the body, every material point is identified by its position vector, $\boldsymbol{x}$, its incremental volume, V, and a mass density of $\rho(\boldsymbol{x})$. Each of the material points can be subjected to body loads, displacement or velocity, which results in motion and consequently deformation. The position vector of material point i in the undeformed state is represented by $\boldsymbol{x}_i$, and it experiences a displacement of $\boldsymbol{u}_i$, which puts it at its new position in the deformed state, expressed as $\boldsymbol{y}_i$. Also, the body load vector applied at material point i is shown as $\boldsymbol{b}_i$. Figure 2.2 depicts the undeformed and deformed states of the body and the relationships among the positions vectors and the displacement vectors of two arbitrary particles i and j. Material points i

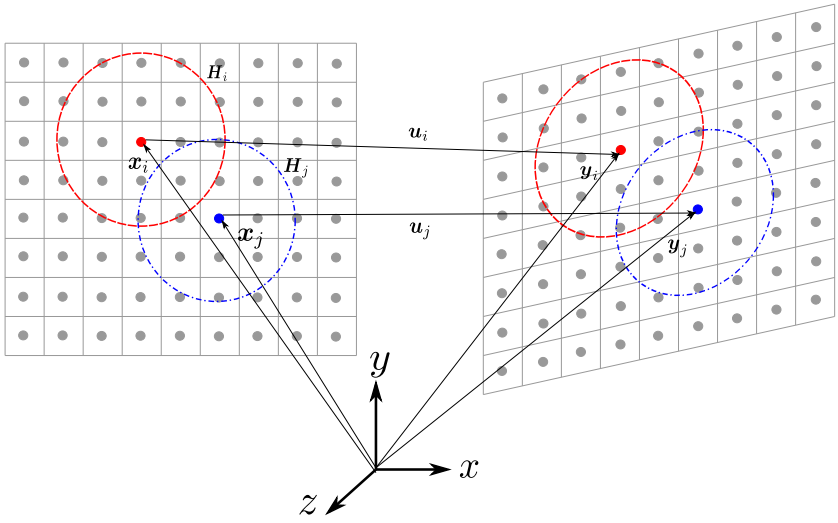

Figure 2.2: Undeformed and deformed states of the body (regenerated from [Madenci and Oterkus(2014)])

and j have a relative position vector $(\boldsymbol{x}_j - \boldsymbol{x}_i)$ in the undeformed stated, but as they experience a deformation, this relative position vector becomes $(\boldsymbol{y}_j - \boldsymbol{y}_i)$ in the deformed configuration. Therefore, in general, the stretch between the two particles located at $\boldsymbol{x}$ and $\boldsymbol{x}'$ can be defined as:

$$s = \frac{|\boldsymbol{y}' - \boldsymbol{y}| - |\boldsymbol{x}' - \boldsymbol{x}|}{|\boldsymbol{x}' - \boldsymbol{x}|} \tag{2.2}$$

2.2 Force density

Material point i interacts with all of the particles within its family, H_i, and is affected by the collective deformation of all of them, thus resulting in a force density vector $\boldsymbol{t}$. In other words, the pairwise interaction force density between material points $\boldsymbol{x}$ and $\boldsymbol{x'}$ is denoted by $\boldsymbol{t}(\boldsymbol{x}' - \boldsymbol{x}, \boldsymbol{u}' - \boldsymbol{u}, t)$. This force density is a function of the relative position vector, $\boldsymbol{x}' - \boldsymbol{x}$, and relative displacement vector, $\boldsymbol{u}' - \boldsymbol{u}$.

2.3 Strain energy density

As a result of the interactions between material points $\boldsymbol{x}$ and $\boldsymbol{x}'$ in a family, a scalar valued micropotential, $w(\boldsymbol{x}' - \boldsymbol{x}, \boldsymbol{u}' - \boldsymbol{u})$ develops, which depends on the material properties, as well as the stretch between $\boldsymbol{x}$ and $\boldsymbol{x}'$. In other words, the micropotential is the energy stored on a single bond. It is worth mentioning that micropotentials have a unit of energy per volume squared. Hence, the strain energy density of a material point at $\boldsymbol{x}$, $W(\boldsymbol{x})$, can be expressed as a summation of micropotentials, $w(\boldsymbol{x}' - \boldsymbol{x}, \boldsymbol{u}' - \boldsymbol{u})$, arising from the interactions of material point $\boldsymbol{x}$ with other particles in its family:

$$W(\boldsymbol{x}, t) = \frac{1}{2} \int_H \frac{1}{2} \left(w(\boldsymbol{x}' - \boldsymbol{x}, \boldsymbol{u}' - \boldsymbol{u}) + w(\boldsymbol{x} - \boldsymbol{x}', \boldsymbol{u} - \boldsymbol{u}') \right) dH \tag{2.3}$$

In (2.3), the domain of integration, H, includes all the material points that interact with material point $\boldsymbol{x}$ and can be defined as:

$$H = \{\boldsymbol{x} \in \beta : ||\boldsymbol{x}' - \boldsymbol{x}|| \leq \delta\} \tag{2.4}$$

Finally, integrating the strain energy density over the domain of the body, β, the

total strain energy of the body, U, can be calculated as:

$$U = \int_{\beta} W(\boldsymbol{x}, t) d\beta \tag{2.5}$$

2.4 Equation of motion

The total kinetic and potential energies of the body can be calculated by summing the kinetic and potential energies of all the material points, respectively. Note that the total potential energy of an elastic body is defined as the sum of total strain energy and the work potential. The kinetic and potential terms are represented in the summation form instead of integration for simplicity. The kinetic and potential of the body can be expressed, respectively as follows:

$$T = \sum_{i=1}^{\infty} \frac{1}{2} \rho_i \dot{\boldsymbol{u}}_i \cdot \dot{\boldsymbol{u}}_i V_i \tag{2.6}$$

$$P = \sum_{i=1}^{\infty} W_i V_i - \sum_{i=1}^{\infty} (\boldsymbol{b}_i \cdot \boldsymbol{u}_i) V_i \tag{2.7}$$

where $\dot{\boldsymbol{u}}_i$ is the velocity vector of material point $\boldsymbol{x}$, and V_i is its volume.
The strain energy density in (2.3) can be reformed as:

$$W_i = \frac{1}{2} \sum_{j=1}^{\infty} \frac{1}{2} (w_{ij} + w_{ji}) V_j \tag{2.8}$$

where w_{ij} is the micropotential of material point i due to its interaction with material points j, and w_{ji} is the micropotential of material point j due to its interaction with material points i. Therefore, by substituting (2.8) into (2.7), the potential energy can be rewritten as:

$$P = \sum_{i=1}^{\infty} \left\{ \frac{1}{2} \sum_{j=1}^{\infty} \frac{1}{2} (w_{ij} + w_{ji}) V_j - (\boldsymbol{b}_i \cdot \boldsymbol{u}_i) \right\} V_i \tag{2.9}$$

Afterwards, by calculating the Lagrangian as $L = T - P$ and applying the Lagrange's equation in (2.13), the equation of motion of material point i can be finally obtained

as:

$$\rho_i \ddot{\boldsymbol{u}}_i = \sum_{i=1}^{\infty} \left[\boldsymbol{t}_{ij}(\boldsymbol{x}_j - \boldsymbol{x}_i, \boldsymbol{u}_j - \boldsymbol{u}_i, t) - \boldsymbol{t}_{ji}(\boldsymbol{x}_i - \boldsymbol{x}_j, \boldsymbol{u}_i - \boldsymbol{u}_j, t) \right] V_i + \boldsymbol{b}_i \tag{2.10}$$

where

$$\boldsymbol{t}_{ij} = \frac{1}{2}\frac{1}{V_j}\left(\sum_{v=1}^{\infty} \frac{\partial w_{iv}}{\partial(\boldsymbol{y}_j - \boldsymbol{y}_i)} V_v \right) \tag{2.11}$$

$$\boldsymbol{t}_{ji} = \frac{1}{2}\frac{1}{V_i}\left(\sum_{v=1}^{\infty} \frac{\partial w_{jv}}{\partial(\boldsymbol{y}_i - \boldsymbol{y}_j)} V_v \right) \tag{2.12}$$

$$\frac{d}{dt}\left(\frac{\partial L}{\partial \dot{\boldsymbol{u}}_j} \right) - \frac{\partial L}{\partial \boldsymbol{u}_j} = 0 \tag{2.13}$$

Lastly, the equation of motion of a particle located at $\boldsymbol{x}$ can be expressed in integral form as:

$$\rho(\boldsymbol{x})\ddot{\boldsymbol{u}}(\boldsymbol{x}, t) = \int_H \left(\boldsymbol{t}(\boldsymbol{x}' - \boldsymbol{x}, \boldsymbol{u}' - \boldsymbol{u}, t) - \boldsymbol{t}(\boldsymbol{x} - \boldsymbol{x}', \boldsymbol{u} - \boldsymbol{u}', t) \right) dH + \boldsymbol{b}(\boldsymbol{x}, t) \tag{2.14}$$

2.5 Boundary conditions

Since peridynamics uses integro-differential equations to define the equations of motion, unlike the classical continuum mechanics theory where partial differential equations are utilized, the application of boundary conditions is performed differently. The tractions or point forces cannot be applied as boundary conditions since their volume integrations result in a zero volume [Madenci and Oterkus(2014)]. Therefore, the external loads can be applied as body force densities in a real material layer along the boundary of a nonzero volume. The thickness of this layer should be comparable to the size of the horizon [Macek and Silling(2007)].

2.6 Balance laws

The linear momentum, $\boldsymbol{M}$, and angular momentum about the coordinate origin, $\boldsymbol{H}_o$, of a set of particles at time, t, and volume, V, are given respectively by:

$$\boldsymbol{M} = \int_V \rho(\boldsymbol{x})\dot{\boldsymbol{u}}(\boldsymbol{x}, t) dV \tag{2.15}$$

$$\boldsymbol{H}_o = \int_V \boldsymbol{y}(\boldsymbol{x},t) \times \rho(\boldsymbol{x}) \dot{\boldsymbol{u}}(\boldsymbol{x},t) dV \tag{2.16}$$

The total force, $\boldsymbol{F}$, and total torque, $\boldsymbol{\Pi_o}$, about the origin can be obtained using the PD formulation as:

$$\boldsymbol{F} = \int_V \boldsymbol{b}(\boldsymbol{x},t) dV + \int_V \int_H \boldsymbol{t}(\boldsymbol{x}' - \boldsymbol{x}, \boldsymbol{u}' - \boldsymbol{u}, t) dH dV - \int_V \int_H \boldsymbol{t}(\boldsymbol{x} - \boldsymbol{x}', \boldsymbol{u} - \boldsymbol{u}', t) dH dV \tag{2.17}$$

$$\begin{aligned} \boldsymbol{\Pi_o} = \int_V \boldsymbol{y}(\boldsymbol{x},t) \times \boldsymbol{b}(\boldsymbol{x},t) dV + \int_V \int_H \boldsymbol{y}(\boldsymbol{x},t) \times \boldsymbol{t}(\boldsymbol{x}' - \boldsymbol{x}, \boldsymbol{u}' - \boldsymbol{u}, t) dH dV - \\ \int_V \int_H \boldsymbol{y}(\boldsymbol{x},t) \times \boldsymbol{t}(\boldsymbol{x} - \boldsymbol{x}', \boldsymbol{u} - \boldsymbol{u}', t) dH dV \end{aligned} \tag{2.18}$$

Eventually, by following $\dot{\boldsymbol{M}} = \boldsymbol{F}$, the balance of linear momentum can be expressed as:

$$\int_V \left(\rho(\boldsymbol{x}) \ddot{\boldsymbol{u}}(\boldsymbol{x},t) - \boldsymbol{b}(\boldsymbol{x},t) \right) dV = 0 \tag{2.19}$$

The details on obtaining the above equation, and the angular momentum are provided in Appendix A. Note that $\boldsymbol{b}$ contains all the external forces including traction, which can be transformed into body forces as explained in 2.5.

Equation (2.19) is automatically satisfied for any interaction force, $\boldsymbol{t}(\boldsymbol{x}' - \boldsymbol{x}, \boldsymbol{u}' - \boldsymbol{u}, t)$ and $\boldsymbol{t}(\boldsymbol{x} - \boldsymbol{x}', \boldsymbol{u} - \boldsymbol{u}', t)$.

By considering only the material points within the horizon, and invoking the balance of linear momentum in (2.19), the balance of angular momentum derived in (A.4) can be finally recast as:

$$\int_H \left((\boldsymbol{y}' - \boldsymbol{y}) \times \boldsymbol{t}(\boldsymbol{x}' - \boldsymbol{x}, \boldsymbol{u}' - \boldsymbol{u}, t) \right) dH = 0 \tag{2.20}$$

It is evident that in order to satisfy (2.20), $\boldsymbol{t}(\boldsymbol{x}' - \boldsymbol{x}, \boldsymbol{u}' - \boldsymbol{u}, t)$ and $\boldsymbol{t}(\boldsymbol{x} - \boldsymbol{x}', \boldsymbol{u} - \boldsymbol{u}', t)$ must be aligned with the relative position vector in the deformed configuration, $(\boldsymbol{y}' - \boldsymbol{y})$. However, the general form that satisfies (2.20) can be derived in terms of the deformation gradient and stress tensors of classical continuum mechanics[Madenci and Oterkus(2014)]. The former approach is the basis of the bond-based Peridynamics, which is covered in Section 2.7, and the later leads to state-based formulation.

2.7 Bond-based Peridynamics

There are two main groups of peridynamic formulation as bond-based and state-based PD. The former formulation accounts for the interaction of material point $\boldsymbol{x}$ and its family members $\boldsymbol{x'}$ in a pairwise manner, which results in less number of independent material constants. Figure 2.3 illustrates a schematic of bond-based PD. However, in state-based PD, the interaction force vectors can have different directions and magnitudes, since these forces rely on the deformation state of all family members of $\boldsymbol{x}$ and $\boldsymbol{x'}$ (Figure 2.4). In this study, the bond-based PD is adopted due to its simplicity for coding implementation.

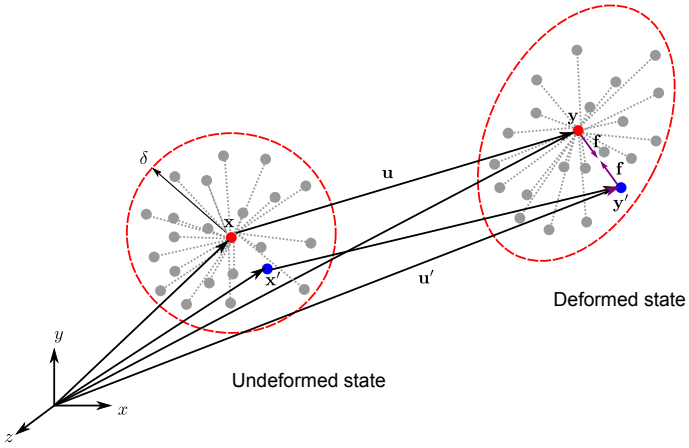

Figure 2.3: Deformation of material points $\mathbf{x}$ and $\mathbf{x}'$ in bond-based formulation (regenerated from [Madenci and Oterkus(2014)])

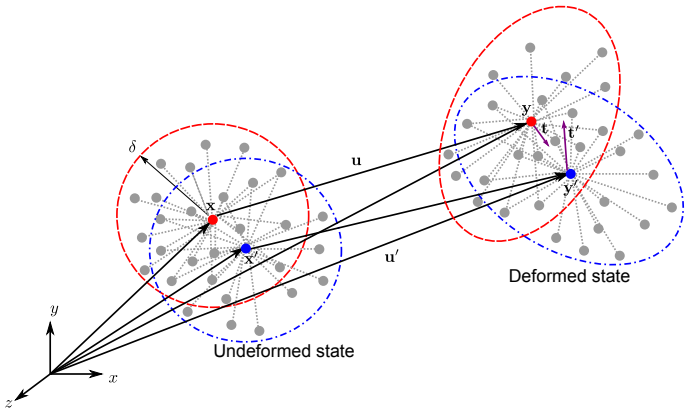

Figure 2.4: Deformation of material points $\mathbf{x}$ and $\mathbf{x}'$ in state-based formulation (regenerated from [Madenci and Oterkus(2014)])

Accordingly, the force density in bond-based PD can be expressed as:

$$\boldsymbol{t}(\boldsymbol{x}'-\boldsymbol{x},\boldsymbol{u}'-\boldsymbol{u},t)=\frac{1}{2}C\frac{\boldsymbol{y}'-\boldsymbol{y}}{|\boldsymbol{y}'-\boldsymbol{y}|}=\frac{1}{2}\boldsymbol{f}(\boldsymbol{x}'-\boldsymbol{x},\boldsymbol{u}'-\boldsymbol{u},t) \tag{2.21}$$

Similarly one can have:

$$\boldsymbol{t}(\boldsymbol{x}-\boldsymbol{x}',\boldsymbol{u}-\boldsymbol{u}',t)=-\frac{1}{2}C\frac{\boldsymbol{y}'-\boldsymbol{y}}{|\boldsymbol{y}'-\boldsymbol{y}|}=-\frac{1}{2}\boldsymbol{f}(\boldsymbol{x}'-\boldsymbol{x},\boldsymbol{u}'-\boldsymbol{u},t) \tag{2.22}$$

Thereby, the equation of motion in (2.14) can be recast for bond-based Peridynamics as:

$$\rho(\boldsymbol{x})\ddot{\boldsymbol{u}}(\boldsymbol{x},t)=\int_H \boldsymbol{f}(\boldsymbol{x}'-\boldsymbol{x},\boldsymbol{u}'-\boldsymbol{u},t)dH+\boldsymbol{b}(\boldsymbol{x},t) \tag{2.23}$$

To satisfy the angular momentum balance law, in bond-based PD, it is assumed that the interaction force is along the same direction as the relative position of the two material points in the deformed configuration, $\boldsymbol{y}'-\boldsymbol{y}=(\boldsymbol{x}'+\boldsymbol{u}')-(\boldsymbol{x}+\boldsymbol{u})$, and is linearly dependent on the stretch between the two material points.
Hence, for an elastic material, the PD force can be expressed as:

$$\boldsymbol{f}=cs\frac{\boldsymbol{y}'-\boldsymbol{y}}{|\boldsymbol{y}'-\boldsymbol{y}|} \tag{2.24}$$

The material parameter, c, also known as bond constant, can be found through equating the strain energy densities of the PD and CCM theories for a material point due to simple loadings, including isotropic expansion and simple shear. This matter is discussed in Section 2.7.1.

Moreover, it is noteworthy that the strain energy density in (2.3) can be recast for bond-based formulation as:

$$W(\boldsymbol{x},t)=\frac{1}{2}\int_H w(\boldsymbol{x}'-\boldsymbol{x},\boldsymbol{u}'-\boldsymbol{u},t)dH \tag{2.25}$$

where the micropotential, $w(\boldsymbol{x}'-\boldsymbol{x},\boldsymbol{u}'-\boldsymbol{u},t)$ is defined as [Silling and Askari(2005)]:

$$w(\boldsymbol{x}'-\boldsymbol{x},\boldsymbol{u}'-\boldsymbol{u},t)=\frac{1}{2}cs^2|\boldsymbol{x}'-\boldsymbol{x}| \tag{2.26}$$

2.7.1 Bond-based Peridynamics for isotropic materials in 2D analysis

Parameter c in (2.24) is an unknown auxiliary parameter that depends on the engineering material constants, pairwise stretch between $\boldsymbol{x}$ and $\boldsymbol{x}'$, and the horizon. Furthermore, it is common to simplify the geometry of a body in order to reduce the computational effort. For instance, long bars can be treated as 1D structures, or thin plates can be assumed to be a 2D structure. Therefore, it is evident that the PD material constants must reflect these idealizations. The focus of this work is on topology optimization of thin plates. As a result, only 2D Peridynamic analysis are studied in this section.

A 2D plate can be dircretized with a single layer of material points along the thickness. Thus, the spherical domain of integral over the family, H, becomes a disk with radius, δ, and thickness, h.

Two different loading cases including an isotropic expansion and a simple shear can be considered to determine the PD constant.

1. **Isotropic expansion**

   An isotropic expansion can be achieved by an equal normal strain of ς in all directions. Note that the thermal expansion effect is neglected here for simplicity. Based on classical continuum mechanics, the stress vector, $\boldsymbol{\sigma}_i$, and the strain vector, $\boldsymbol{\varepsilon}_i$, at $\boldsymbol{x_i}$, under two-dimensional idealization respectively are:

$$\boldsymbol{\sigma}_i^T = \{\sigma_{xx(i)}\ \sigma_{yy(i)}\ \sigma_{xy(i)}\} \tag{2.27}$$

$$\boldsymbol{\varepsilon}_i^T = \{\varepsilon_{xx(i)}\ \varepsilon_{yy(i)}\ \varepsilon_{xy(i)}\} \tag{2.28}$$

   For an isotropic material with bulk modulus, κ, and shear modulus, μ, one can write the following from classical continuum mechanics:

$$\boldsymbol{\sigma}_i = \mathbf{C}\boldsymbol{\varepsilon}_i \tag{2.29}$$

where the material property matrix, $\mathbf{C}$ is defined as:

$$\mathbf{C} = \begin{bmatrix} \kappa+\mu & \kappa-\mu & 0 \\ \kappa-\mu & \kappa+\mu & 0 \\ 0 & 0 & \mu \end{bmatrix} \tag{2.30}$$

Hence, the strain components in body are:

$$\varepsilon_{xx(i)} = \varepsilon_{yy(i)} = \varsigma, \quad \gamma_{xy(i)} = 0 \tag{2.31}$$

Therefore, using equations (2.27) to (2.31), the strain energy density and the dilatation terms from CCM are as follows, respectively:

$$W_i = \frac{\kappa}{2}\Theta_i^2 + \frac{1}{4\mu}(\sigma_{xx(i)}^2 + \sigma_{yy(i)}^2) + \frac{1}{2\mu}\sigma_{xy(i)}^2 = 2\kappa\varsigma^2 \tag{2.32}$$

$$\Theta_i = \varepsilon_{xx(i)} + \varepsilon_{yy(i)} = 2\varsigma \tag{2.33}$$

According to [Madenci and Oterkus(2014)], in the case of isotropic expansion, the relative position vector between the material points $\boldsymbol{x}_i$ and $\boldsymbol{x}_j$ in the deformed configuration becomes:

$$|\boldsymbol{y}_j - \boldsymbol{y}_i| = (1+\varsigma)|\boldsymbol{x}_j - \boldsymbol{x}_i| \tag{2.34}$$

For an isotropic and elastic material, the explicit form of the strain energy density, W_i, can be obtained by generalizing the expression for the **local theory**, as:

$$W_i = a\Theta_i^2 - b\sum_{j=1}^{N_f} \varpi_{ij}\left(|\boldsymbol{y}_j - \boldsymbol{y}_i| - |\boldsymbol{x}_j - \boldsymbol{x}_i|\right) V_j \tag{2.35}$$

Similarly, the generalized expression of dilatation, Θ_i for the **local theory** can be obtained as:

$$\Theta_i = d\sum_{j=1}^{N_f} \varpi_{ij} s_{ij} \frac{\boldsymbol{y}_j - \boldsymbol{y}_i}{|\boldsymbol{y}_j - \boldsymbol{y}_i|} \cdot (\boldsymbol{x}_j - \boldsymbol{x}_i) V_j \tag{2.36}$$

where $\varpi_{ij} = \varpi\left(|\boldsymbol{x}_j - \boldsymbol{x}_i|\right)$ is the nondimensional influence function, providing

a tool to take into consideration the affect of particles far from the current material point at $\boldsymbol{x}_i$. It can be shown that for bond-based PD, the value of ϖ_{ij} is equal to $\frac{\delta}{\xi}$, where $\xi = |\boldsymbol{\xi}| = |\boldsymbol{x}_j - \boldsymbol{x}_i|$. Also, parameters a, b, and d are other material constants that need to be found besides c in (2.24).

Therefore, by substituting the CCM values of the dilatation term, Θ_i from (2.33), the relative position vector from (2.34), and the influence function, ϖ_{ij} into (2.35), the strain energy at material point $\boldsymbol{x}_i$, which interacts with other material points in its family can be evaluated when changing the summation into an integral term over a disk of radius, δ, and thickness, h, as:

$$W_i = a(2\varsigma)^2 + \frac{2}{3}\pi b h \delta^4 \varsigma^2 \tag{2.37}$$

Now, by equating the strain energy density of material point at $\boldsymbol{x}_i$ obtained from classical continuum mechanics, (2.32), and the strain energy density obtained from Peridynamics, (2.37) a relationship between the PD parameters and engineering material constants can be established as follows:

$$4a + \frac{2}{3}\pi b h \delta^4 = 2\kappa \tag{2.38}$$

Likewise, the dilatation term in (2.36) can be calculated as:

$$\Theta_i = \pi h d \delta^3 \varsigma \tag{2.39}$$

Moreover, by equating (2.33) and (2.39), the PD parameter, d can be expressed as:

$$d = \frac{2}{\pi h \delta^3} \tag{2.40}$$

The isotropic expansion could provide two equations; (2.38), and (2.40). However, two more equations are still required to determine the four Peridynamic unknowns parameters. These extra equations can be obtained by studying a simple shear loading case.

2. **Simple shear**

   A simple shear can be applied by:

$$\varepsilon_{xx(i)} = \varepsilon_{yy(i)} = 0, \quad \gamma_{xy(i)} = \varsigma \tag{2.41}$$

As a result, Therefore, using equations (2.27) to (2.30), plus (2.41), one has:

$$W_i = \frac{\kappa}{2}\Theta_i^2 + \frac{1}{4\mu}(\sigma_{xx(i)}^2 + \sigma_{yy(i)}^2) + \frac{1}{2\mu}\sigma_{xy(i)}^2 = \frac{1}{2}\mu\varsigma^2 \tag{2.42}$$

$$\Theta_i = \varepsilon_{xx(i)} + \varepsilon_{yy(i)} = 0 \tag{2.43}$$

According to Figure (2.5), the relative position vector in the deformed state for a simple shear loading can be evaluated as the following:

$$|\boldsymbol{y}_j - \boldsymbol{y}_i| = [1 + sin\theta cos\theta\varsigma]|\boldsymbol{x}_j - \boldsymbol{x}_i| \tag{2.44}$$

By utilizing (2.35) from local theory, and changing the summation into an

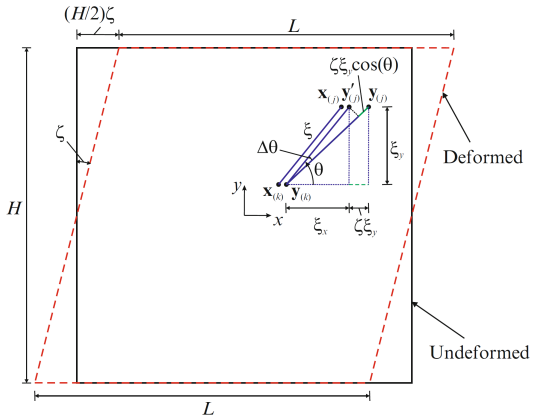

Figure 2.5: A schematic of a 2D plate deformation under simple shear [Madenci and Oterkus(2014)]

integral, the expression for the strain energy density of simple shear loading can be obtained as:

$$W_i = \frac{\pi h \delta^4 \varsigma^2}{12} b \tag{2.45}$$

Hence, equating (2.45) obtained from Peridynamics and (2.42) from CCM will result in another relationship between a PD parameter, b, and engineering material constants:

$$b = \frac{6\mu}{\pi h \delta^4} \tag{2.46}$$

Substituting for b in (2.38) leads to:

$$a = \frac{1}{2}(\kappa - 2\mu) \tag{2.47}$$

However, one more equation is necessary to find the last PD parameter, c. It can be shown that for bond-based Peridynamics, the ratio of c over b is equal to four times the horizon, δ [Madenci and Oterkus(2014)]. Therefore:

$$c = \frac{24\mu}{\pi h \delta^3} = \frac{9E}{\pi h \delta^3} \tag{2.48}$$

where E is the elastic modulus. Note that, in the case of bond-based PD, the strain energy equilibrium between CCM and PD results in the Poisson's ratio, ν of 1/3 [Madenci and Oterkus(2014)].

2.8 Cracks

In order to consider the existence of cracks and their influence on the behaviour of the structure, the PD bonds between the material points the line of action of which passes through the crack surface are broken. Figure 2.6 displays a schematic of the broken bonds (in red), which have an intersection with the crack surface. It should be

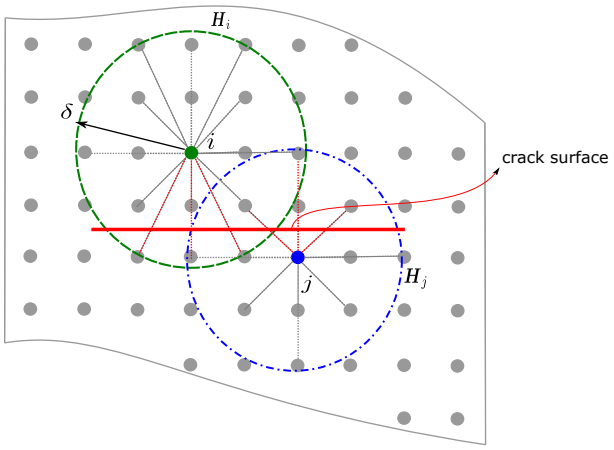

Figure 2.6: Broken PD bonds (in red) due to the existence of a crack

noted that, the cracks considered in this study, can not propagate, or new cracks can not initiate.

2.9 Numerical solution method

The PD equation of motion in (2.23), is an integro-differential equation. Therefore, the solution to this equation can be conducted through numerical techniques for spatial

and time integration.

2.9.1 Spatial integration

The spatial integration can be performed by utilizing a meshless method due to its simplicity. Additionally, it serves as a useful discretization strategy for modelling discontinuities such as cracks, voids, etc. Hence, the domain can be divided into a finite number of subdomains (e.g., quadrilateral for 2-D regions). After discretization, the material points associated with specific volumes are placed in the subdomains. Consequently, the volume integration in (2.23) can be approximated as:

$$\rho(\boldsymbol{x}_i)\ddot{\boldsymbol{u}}(\boldsymbol{x}_i,t) = \sum_{j=1}^{N_f} \boldsymbol{f}(\boldsymbol{x}_j - \boldsymbol{x}_i, \boldsymbol{u}(\boldsymbol{x}_j,t) - \boldsymbol{u}(\boldsymbol{x}_i,t))V_j + \boldsymbol{b}(\boldsymbol{x}_i,t) \tag{2.49}$$

where $\boldsymbol{x}_i$ and $\boldsymbol{x}_j$ are the position vectors located at the ith and jth material points, respectively. N_f is the number of family members of particle i, j is a material point inside the family of material point i and V_j represents the volume of material point j. Note that in (2.49), it is assumed that the domain is discretized into square subdomains and in each subdomain, there is only one particle.

Similarly, the strain energy density of the material point i can be expressed in the discrete form as follows:

$$W(\boldsymbol{x}_i,t) = \frac{1}{2}\sum_{j=1}^{N_f} w(\boldsymbol{x}_j - \boldsymbol{x}_i, \boldsymbol{u}(\boldsymbol{x}_j,t) - \boldsymbol{u}(\boldsymbol{x}_i,t))V_j \tag{2.50}$$

2.9.2 Time integration

The equation of motion in (2.49) is dynamic because of the existence of the inertia term. In this study, we are focusing on quasi-static loadings, therefore, the inertia term can be neglected, and there is no need for time integration, consequently.

The adaptive dynamic relaxation (ADR) method introduced in [Madenci and Oterkus(2014), Underwood(1983)] has been widely used to transform the dynamic PD equation of motion into a quasi-static or static problem. The ADR method is based on the fact that the static solution is the steady-state part of the transient response of the solution. Although ADR may be a robust technique, attaining a static condition can take several numbers of time steps as it imposes fictitious damping to the system to guide to the the steady-state solution. As a result, this method

can significantly increase the computational time and may not be very suitable for optimization problems. Hence, the direct solution method is used here as an alternative. This approach is not as computationally expensive as the ADR method, which makes it useful for topology optimization problems. According to [Silling(2010)], the PD force density given in (2.24) can be linearized for material point i when using the bond-based formulation as follows:

$$\boldsymbol{f}(\boldsymbol{x}_j - \boldsymbol{x}_i, \boldsymbol{u}(\boldsymbol{x}_j, t) - \boldsymbol{u}(\boldsymbol{x}_i, t)) \equiv \boldsymbol{f}_{ij} \equiv \boldsymbol{f}(\boldsymbol{\xi}_{ij}, \boldsymbol{\eta}_{ij}, t) = c\frac{\boldsymbol{\xi}_{ij} \otimes \boldsymbol{\xi}_{ij}}{|\boldsymbol{\xi}_{ij}|^3}\boldsymbol{\eta}_{ij} = \frac{c}{|\boldsymbol{\xi}_{ij}|}\mathbf{R}_{ij}\boldsymbol{\eta}_{ij} \tag{2.51}$$

where $\boldsymbol{\eta}_{ij} = \boldsymbol{u}(\boldsymbol{x}_j, t) - \boldsymbol{u}(\boldsymbol{x}_i, t)$, is the relative displacement vector between material points i and j, and $\otimes$ represents the dyadic product. The matrix $\mathbf{R}_{ij}$ is a transformation matrix to associate the relative displacement vector, η_{ij}, with the bond direction in the un-deformed configuration. Hence, this matrix for 2-D analysis can be defined as:

$$\mathbf{R}_{ij} = \begin{bmatrix} \cos^2\phi_{ij} & \cos\phi_{ij}\sin\phi_{ij} \\ \cos\phi_{ij}\sin\phi_{ij} & \sin^2\phi_{ij} \end{bmatrix} \tag{2.52}$$

where ϕ_{ij} represents the direction of the unite vector of the relative position vector in the un-deformed configuration, ξ_{ij}. In other words:

$$\frac{\boldsymbol{\xi}_{ij}}{|\boldsymbol{\xi}_{ij}|} = \begin{pmatrix} \cos\phi_{ij} \\ \sin\phi_{ij} \end{pmatrix} \tag{2.53}$$

By substituting (2.51) into (2.49) and setting the acceleration term to zero, the PD equation of motion can be rewritten as:

$$\sum_{j=1}^{N_f} \frac{c}{|\boldsymbol{\xi}_{ij}|}\mathbf{R}_{ij}\boldsymbol{\eta}_{ij}V_j + \boldsymbol{b}_i = 0 \tag{2.54}$$

Also, (2.54) can be expressed in an alternative form as:

$$\sum_{j=1}^{N_f} \frac{c}{|\boldsymbol{\xi}_{ij}|}[\mathbf{R}_{ij} \ -\mathbf{R}_{ij}] \begin{pmatrix} \boldsymbol{u}_i \\ \boldsymbol{u}_j \end{pmatrix} V_j = \boldsymbol{b}_i \tag{2.55}$$

which can be written in the form of compact matrix-vector representation as:

$$\mathbf{k}_i\boldsymbol{d}_i = \boldsymbol{b}_i \tag{2.56}$$

where $\mathbf{k}_i$ is the local stiffness matrix for particle i and can be explicitly defined as:

$$\mathbf{k}_i = \left[\mathbf{R}_{i1} \frac{c}{|\boldsymbol{\xi}_{i1}|} V_1 + \cdots + \mathbf{R}_{iN_f} \frac{c}{|\boldsymbol{\xi}_{iN_f}|} V_{N_f} \;\; - \mathbf{R}_{i1} \frac{c}{|\boldsymbol{\xi}_{i1}|} V_1 \;\; \cdots \;\; - \mathbf{R}_{iN_f} \frac{c}{|\boldsymbol{\xi}_{iN_f}|} V_{N_f} \right] \tag{2.57}$$

And $\boldsymbol{d}_i$ is the displacement vector:

$$\boldsymbol{d}_i = \begin{Bmatrix} \boldsymbol{u}_i \\ \boldsymbol{u}_1 \\ \vdots \\ \boldsymbol{u}_{N_f} \end{Bmatrix} \tag{2.58}$$

Note that each of the elements of $\boldsymbol{d}_i$ contains the x and y components of the displacement vector of material point i and the particles located within its horizon. That is:

$$\boldsymbol{u}_o = \begin{Bmatrix} \boldsymbol{u}_o^x \\ \boldsymbol{u}_o^y \end{Bmatrix} \quad (o = i, 1, \cdots, N_f) \tag{2.59}$$

The PD equation of motion for the quasi-static case can be obtained as a single matrix-vector equation in the total domain β by assembling all the local stiffness matrices for all the material points in the body, expressed in (2.56) as:

$$\mathbf{K}\mathbf{d} = \mathbf{b} \tag{2.60}$$

where

$$\mathbf{K} = \bigcup_{i=1}^{N} \mathbf{k}_i = \begin{bmatrix} \mathbf{k}_1 & \cdots & 0 \\ \vdots & \ddots & \vdots \\ 0 & \cdots & \mathbf{k}_N \end{bmatrix} \tag{2.61}$$

$$\mathbf{d} = \bigcup_{i=1}^{N} \boldsymbol{d}_i = \begin{Bmatrix} \boldsymbol{d}_1 \\ \vdots \\ \boldsymbol{d}_N \end{Bmatrix} \tag{2.62}$$

$$\mathbf{b} = \bigcup_{i=1}^{N} \boldsymbol{b}_i = \begin{Bmatrix} \boldsymbol{b}_1 \\ \vdots \\ \boldsymbol{b}_N \end{Bmatrix} \tag{2.63}$$

where $\mathbf{K}$, $\mathbf{d}$, and $\mathbf{b}$ are the global stiffness matrix, displacement vector, and force

vector of all material points, respectively. Also, N, is the total number of material points in the body.

Chapter 3

Topology Optimization

A general constrained optimization problem can be expressed as:

$$\min F(\boldsymbol{\alpha}) \tag{3.1a}$$

$$subject\ to: \begin{cases} X_m(\boldsymbol{\alpha}) = 0 & \text{for } m = 1, 2, \cdots, z \\ Y_g(\boldsymbol{\alpha}) \leq 0 & \text{for } g = 1, 2, \cdots, r \end{cases} \tag{3.1b}$$

where $\boldsymbol{\alpha}$ is the vector of unknowns that we seek to find, $F(\boldsymbol{\alpha})$ is the objective function, $X_m(\boldsymbol{\alpha})$ are equality constraints and $Y_g(\boldsymbol{\alpha})$ are inequality constraints. The general cast of the topology optimization problem, which is typically subject to a volume constraint, $G_0 \leq 0$, and possibly r other constraints, $G_g \leq 0,\ g = 1, \cdots, r$ can be written in mathematical form as:

$$\min F(\mathbf{d}(\boldsymbol{\alpha}), \boldsymbol{\alpha}) \tag{3.2a}$$

$$subject\ to: \begin{cases} G_0(\boldsymbol{\alpha}) \leq 0 \\ G_g(\mathbf{d}(\boldsymbol{\alpha}), \boldsymbol{\alpha}) \leq 0 & \text{for } g = 1, 2, \cdots, r \end{cases} \tag{3.2b}$$

where the material distribution in the design domain, Ω is described by $\alpha(\boldsymbol{x}),\ \forall \boldsymbol{x} \in \Omega$, and $\mathbf{d}$ satisfies a linear or non-linear state equation.

A multi-material topology optimization problem can be defined as finding the optimum distribution of $p \in \mathbb{N}$ $(p \geq 2)$ numbers of distinct materials over a fixed nonempty design domain Ω such that a set of constraint(s) are satisfied. In this

work, the objective is to maximize the stiffness of the structure, which is equivalent to minimizing compliance. However, it is worth mentioning that minimizing compliance as a measure of flexibility of the structure in an average manner does not necessarily imply that the maximum displacement at the critical point of the structure is minimized too.

In the present work, the *alternating active-phase algorithm* is adopted to recast the compliance minimization of multi-material structures due to its simplicity and efficiency. This method is discussed extensively in 3.1. The *optimality criteria method* is utilized and explained in 3.2 to solve optimization problem formulated through the alternating active-phase algorithm. Next, the filtering approach used to eliminate numerical instabilities during the optimization process is described in 3.3.

3.1 Alternating Active-Phase Algorithm

The design variables are set to values in the range of 1 and 0 for each of the materials. The material distribution is determined by the local volume fraction fields, α_k^i ($k = 1, 2, \cdots, p;\ i = 1, 2, \cdots, N$) for $p-1$ solid materials, one void phase and N material points. The following upper and lower bounds can be defined for the local volume fractions:

$$l_k \leq \alpha_k^i \leq u_k,\ k = 1, 2, \cdots, p \tag{3.3}$$

where $0 \leq l_k \leq u_k \leq 1$. Since no overlaps and gaps are allowed in the structure, the summation of all of the local volume fractions for each point $\boldsymbol{x} \in \Omega$ should be equal to one. Therefore:

$$\sum_{k=1}^{p} \alpha_k^i = 1 \tag{3.4}$$

Moreover:

$$\int_\Omega \alpha_k^i d\Omega = \Lambda_k,\quad \sum_{k=1}^{p} \Lambda_k = \Lambda_0 \tag{3.5}$$

where Λ_k and Λ_0 are the user-defined volume of the kth phase and the volume of the whole design domain, respectively. In other words, $\Lambda_k = \omega_k \Lambda_0$; where ω_k is the local volume constraint on each phase.

In TO problems, the local material properties are local functions of volume fractions of the contributing phases. In order to compute these properties, the SIMP method is used, which utilizes the power-law interpolation scheme to define the elastic modulus

of material point i as a function of design variables (volume fractions). The SIMP interpolation can be expressed as follows:

$$E_i = \sum_{k=1}^{p} (\alpha_k^i)^q E_k^s \tag{3.6}$$

where q is the penalization factor, and E_k^s is the elastic modulus corresponding to the kth phase.

The motivation for developing the alternating active phase algorithm is to provide a general framework to convert binary phase topology optimization into multi-phase ones by minimal effort and modification, plus, keeping the robustness and the efficiency of the original algorithms [Tavakoli and Mohseni(2014)]. In this method, the optimization calculations are done through inner loops. In each inner loop, a two-phase topology sub-problem is solved by fixing the topologies of $p-2$ phases to the last known values, so that those of the two remaining phases (active phases) can vary. If active phases are denoted by 'χ' and 'ψ', then their volume fraction field, $\tau_{\chi\psi}$, which varies during every binary phase topology optimization sub-problem can be obtained from the following equation:

$$\tau_{\chi\psi}^i = 1 - \sum_{\substack{k=1 \\ k\neq\{\chi,\psi\}}}^{p} \alpha_k^i \tag{3.7}$$

It is only required to take the volume fraction of χ as the design variable of the sub-problem because after solving each of them, the volume fraction of phase ψ (background phase) can be calculated as:

$$\alpha_\psi^i = \tau_{\chi\psi}^i - \alpha_\chi^i \tag{3.8}$$

In each inner loop, the temporary upper bound for phase χ can be modified as:

$$u_\chi^{i,temp} = \min(u_\chi, \tau_{\chi\psi}^i) \tag{3.9}$$

Note that there is no need to modify the lower bound.

Therefore, the internal binary-phase topology optimization solver can be expressed as:

$$\min \Gamma(\boldsymbol{\alpha}_{\chi\psi}^i) \tag{3.10a}$$

$$s.t. \begin{cases} \mathbf{Kd} = \mathbf{b} \\ \int_{\Omega} \alpha_{\chi}^{i} d\Omega = \Lambda_{\chi} \\ E_i = \sum_{k=1}^{p} (\boldsymbol{\alpha}_{\chi\psi}^{i})^q E_k^s \\ l_{\chi}^{i} \leq \alpha_{\chi}^{i} \leq u_{\chi}^{i,temp} \end{cases} \tag{3.10b}$$

where $\boldsymbol{\alpha}_{\chi\psi}^{i} = \left\{\alpha_1^i, \alpha_2^i, \cdots, \alpha_p^i\right\}$ is the design vector in which α_{χ}^{i} and α_{ψ}^{i} could be varied and α_k^i is fixed for $k \neq \{\chi, \psi\}$. The volume constraint of the background phase, ψ, is determined by (3.7) and (3.8). Parameter Γ represents the overall compliance of the structure. Since the value of the total compliance is numerically two times greater than the overall strain energy, we can minimize the strain energy of the structure expressed in (2.5), instead of compliance. Therefore, in (3.10a), parameter Γ can be replaced by the total strain energy, U.

Because of the nonlinear nature of the topology optimization problem, the internal optimization solver uses an iterative algorithm. As a result, it needs a convergence criterion. Here, an infinity norm, $||.||_{\infty}$, of changes in the design vector during two consecutive iterations is used as a criterion. That is, when the maximum of local variations in the volume fractions is smaller than a threshold, the iterations are stopped, and the last design vector is reported as an optimal solution. Besides, an upper bound on the number of iterations can be imposed as a stopping criterion.

It is worth mentioning that the active phase algorithm is based on two assumptions. First, the iterations of the internal sub-problem solver are strictly feasible with respect to all the constraints. Second, in each internal loop, the objective function decreases monotonically as the iterations of the internal algorithm proceed.

According to all the work above, the multi-material topology optimization problem, using active phase algorithm and SIMP method, can be formulated as:

$$\min U = \sum_{i=1}^{N} W(x_i) V_i \tag{3.11a}$$

$$s.t. \begin{cases} \mathbf{Kd} = \mathbf{b} \\ E_i = \sum_{k=1}^{p} (\alpha_k^i)^q E_k^s \\ \sum_{k=1}^{p} \omega_k \Lambda_0 = \Lambda_0 \\ 0 \leq \omega_k \leq 1 \\ 0 \leq \alpha_{min} \leq \alpha_k^i \leq 1 \end{cases} \tag{3.11b}$$

where the value of α_{min} is set to be a very small but non-zero number to avoid the singularity of the structural stiffness matrix.

Also, the active phase algorithm can be summarized in the flowchart illustrated in Figure 3.1, where e indicates the iteration number, and e_{max} is the threshold of the iterations, after which the optimization stops and the latest design variable value is reported as the optimum.

3.1.1 Modification of PD bond constant for the application of multi-material structures

During the topology optimization process, some binary-phase regions containing phases with very different material properties (e.g., void and solid) can appear. On the other hand, the value of the bond-constant in (2.48) is a function of these material properties (here, Young's modulus) and it is obtained by assuming that the material points i and j have the same Young's modulus. Therefore, due to the fact that the contribution of particles i and j is different, it is necessary to consider the influence of their different material properties on the bond connecting them. To do so, a weighting approach proposed in [Cheng et al.(2019)Cheng, Sui, Yin, Yuan, and Chu] for functionally graded materials is utilized in this study. Young's modulus of the two material points can be defined proportional to the effect of the bond as:

$$E_{ij} = \vartheta E_i + \varkappa E_j \tag{3.12}$$

where

$$\vartheta = \frac{E_j}{E_i + E_j}; \quad \varkappa = \frac{E_i}{E_i + E_j} \tag{3.13}$$

By redefining Young's modulus used in (2.48), the bond-constant value is modified. For instance, if material point i is solid and material point j is void such that $E_j \ll E_i$, the

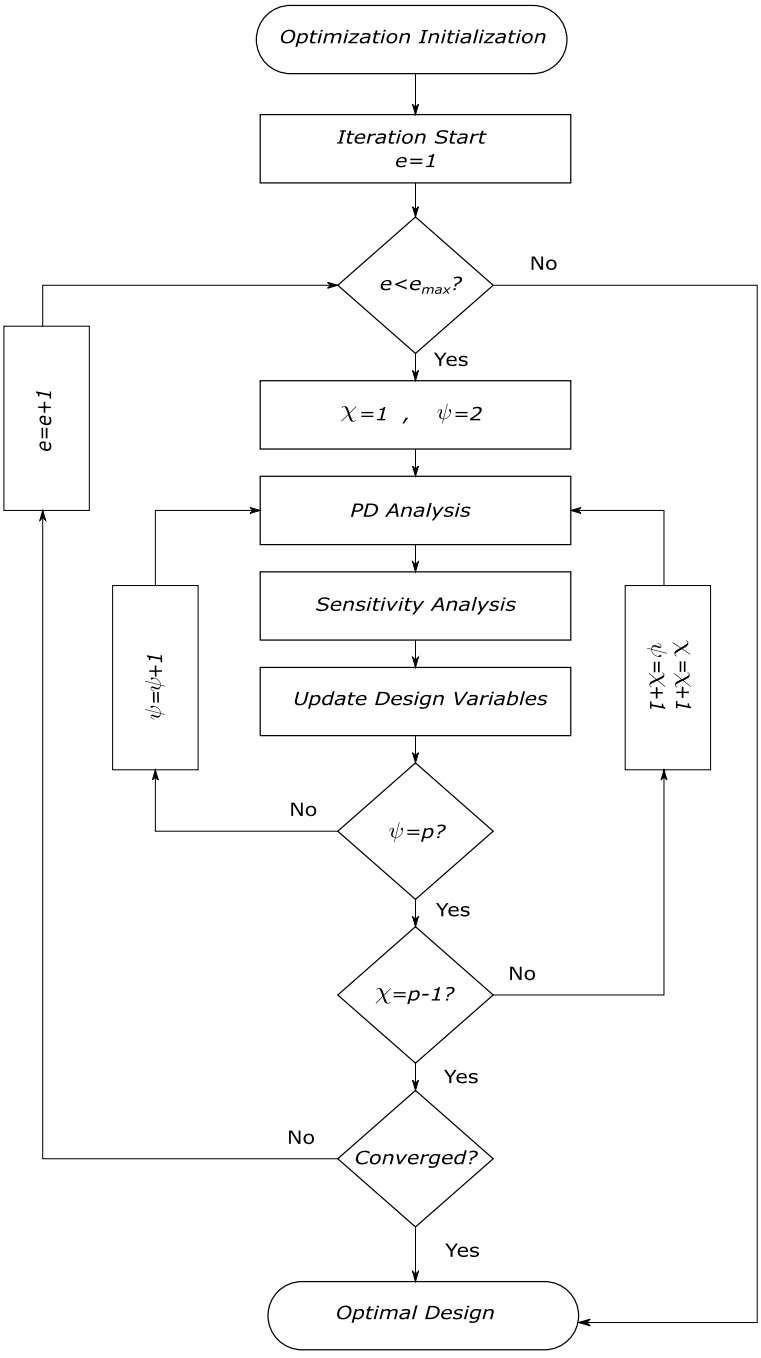

Figure 3.1: flowchart of an alternating active-phase algorithm

value of E_{ij} in (3.12) will converge to E_j. Hence, the magnitude of the bond-constant is negligible, resulting into zero interaction and strain energy density. On the other hand, if the two material points are the same, such that $E_i = E_j$, the value of E_{ij} will converge to E_i which does not result in any alteration in the magnitude of the bond-constant between material points i and j.

3.2 Optimality Criteria Method

The optimization problem in (3.11) can be solved using several different methods such as Optimality Criteria (OC), Sequential Linear Programming (SLP), and so forth. Due to its simplicity, the OC approach [Bendsøe and Bendsøe(1995)] is used in this study. In this method, a heuristic scheme is utilized to update the design variables independently from the updates at other points, based on the necessary conditions of optimality. This update scheme is defined as:

$$\alpha_e^{new} = \begin{cases} \max(0, \alpha_e - M) & \text{if} \quad \alpha_e B_e^{\iota} \leq \max(0, \alpha_e - M) \\ \alpha_e B_e^{\iota} & \text{if} \quad \max(0, \alpha_e - M) \leq \alpha_e B_e^{\iota} \leq \min(1, \alpha_e + M) \\ \min(1, \alpha_e + M) & \text{if} \quad \alpha_e B_e^{\iota} \geq \min(1, \alpha_e + M) \end{cases} \tag{3.14}$$

where M (move) is a positive move-limit which can be chosen by experiment, in order to obtain a suitable, rapid, and stable convergence of the iterations. In (3.14), $\iota(= 1/2)$ is a numerical damping coefficient, and B_e is obtained from the optimality condition for the eth iteration as:

$$B_e = \frac{-\dfrac{\partial U}{\partial \alpha_e}}{\lambda \dfrac{\partial V}{\partial \alpha_e}} \tag{3.15}$$

where λ is the Lagrangian multiplier that must be chosen such that the volume constraint is satisfied. Its appropriate value can be found through a bisection algorithm.

The sensitivities of the objective function, U, and the material point volume, V, with respect to the local volume fractions, can be obtained as:

$$\frac{\partial U}{\partial \alpha_e} = -q(\alpha_e)^{q-1} U_e^s \tag{3.16}$$

$$\frac{\partial V}{\partial \alpha_e} = 1 \tag{3.17}$$

In (3.16), U_e^s is the strain energy of solid particles. According to this equation, it can be stated that the sensitivity of void particles with a negligible value for density is equal to zero when the penalization coefficient, q goes to infinity. In (3.17), it is assumed that each particle has unit volume.

In each inner loop of binary-phase topology optimization, the strain energy of a particle can be stated based on the multiplication of penalized design variable and the strain energy of the solid particle as:

$$U_i = (\alpha_e)^q U_e^s \tag{3.18}$$

where U_i is the strain energy of each particle (i.e. its strain energy density). After finding the solution to the displacement field at each optimization iteration, the particle's strain energy can obtained as:

$$U_i = W(x_i)V_i \tag{3.19}$$

3.3 Filtering

Two types of filtering techniques can be used to eliminate the instabilities and checkerboard patterns: application of a filter to either the sensitivities or the densities. In this work, the former method is adopted. For filtering purposes, a circular sub-domain with the radius of R_{min} is defined at the centroid of the ith particle, which includes a set of neighbor particles, n. These adjacent particles influence the sensitivity of the ith particle proportionately to the distance between these two particles, R_{in}. Using the Shepard interpolation scheme, the modified sensitivities at each particle in the OC approach is as follows:

$$\widehat{\frac{\partial U}{\partial \alpha_i}} = \frac{1}{\alpha_i \sum_{n=1}^{N_i} \varphi(R_{in})} \sum_{n=1}^{N_i} \alpha_n \varphi(R_{in}) \frac{\partial U}{\partial \alpha_n} \tag{3.20}$$

where $R_{in} = |\boldsymbol{x}_n - \boldsymbol{x}_i|$ is the distance between particles i and n, N_i is the total number of particles in the sub-domain of material point i, and $\varphi(R_{in})$ is a weighting function

(convolution operator) defined as:

$$\varphi(R_{in}) = \begin{cases} R_{min} - R_{in} & \text{if} \quad R_{in} \leq R_{min} \\ 0 & \text{if} \quad R_{in} > R_{min} \end{cases} \tag{3.21}$$

Note that the weighting function decays linearly with the distance from material point n. Therefore, instead of the original sensitivity in (3.16), the modified sensitivity obtained in (3.20) is used in the Optimality Criteria update in (3.15). The filter radius can be interpreted as a design constraint; literature shows that the bigger R_{min} is, the thicker the inner links will become. Also, increasing the minimum filter radius can lower the number of the inner links [Kefal et al.(2019)Kefal, Sohouli, Oterkus, Yildiz, and Suleman].

Chapter 4

Examples and Discussions

To investigate the proposed approach , the results of three case studies reported in [Banh and Lee(2018)] are compared against our results. These cases investigate the effect of the direction of an interior crack on the optimal topology of a bridge design domain loaded by a concentrated force. Next, four examples are carried to evaluate the robustness of the current method for multi-material TO problems. The impact of an initially embedded crack on the structure is studied in the *cantilever beam*, *L-shape structure* and the *bridge with uniform pressure load* examples. Furthermore, the problem of multi-material topology optimization is solved using three and four phases for a bridge structure. Moreover, the total displacement and strain energy density distributions are provided for all the case-studies in order to investigate the influence of cracks. In order to have a better presentation of the strain energy density distribution, its mean value is taken as the maximum and any values higher than that are depicted as the maximum.

For all of the examples mentioned above, the value of the penalization factor is assumed to be three. According to [Bendsøe and Sigmund(1999)] when the penalization factor is equal or greater than three, the SIMP model obeys Hashin-Shtrikman bounds and the prevailing of some intermediate densities does not exist. To represent different phases, four colours are used: red, blue, green, and white. As the colours change from red to white, the elastic modulus decreases consecutively with red as the hardest and white the softest materials (i.e. void). It should be noted that all the forces are applied to particles as a body force.

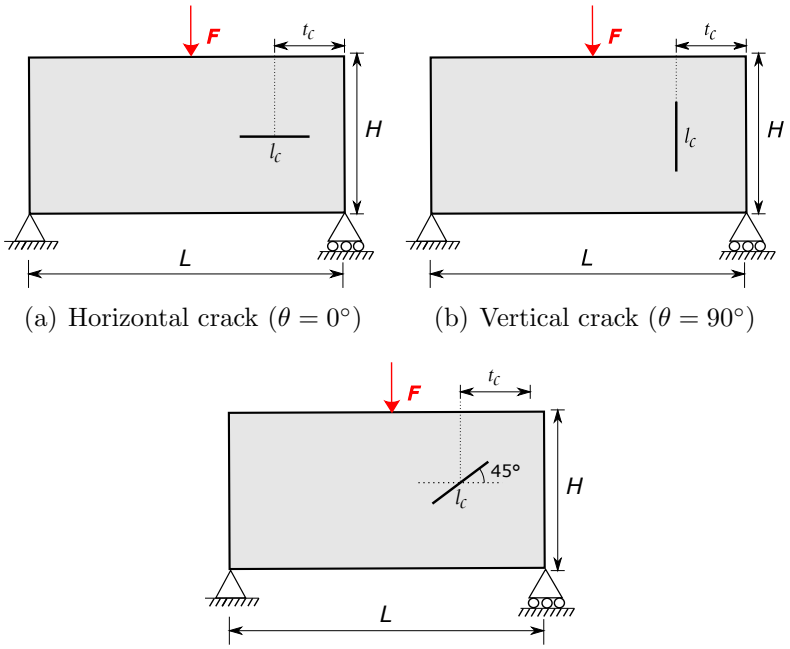

(a) Horizontal crack ($\theta = 0°$) (b) Vertical crack ($\theta = 90°$)

(c) Inclined crack ($\theta = 45°$)

Figure 4.1: Studying the effect of the direction of the interior crack

4.0.1 The effect of the direction of interior cracks

In this case study, the impact of the direction of an interior crack on the optimal topology is investigated in three different orientations: an inclined, a horizontal, and a vertical crack with the same length (Figure 4.1). The length of the crack and its distance from the right edge are: $l_c = 15.5, t_c = 9.25$, respectively. The length of the structure is $L = 40$ and the height is $H = 20$. Accordingly, the design domain is discretized into 40×20 particles. The left bottom corner is fixed and the right bottom corner is simply supported. The magnitude of the applied force at the middle of the upper edge is $F = 200$. The total volume constraint is chosen to be 40%. Moreover, the volume constraint for the hard material ($E = 400 \times 10^3$) is 15% and for the soft material ($E = 200 \times 10^3$) is 25%. To alleviate singularities in the stiffness matrix, the value of Young's modulus of the void phase is considered to be 10. Also, the value of the minimum filter radius is 1.5.

Figure 4.2 displays a comparison between the PD-TO results (left column) with those from [Banh and Lee(2018)], where the alternating active-phase algorithm is used with X-FEM (right column). As it can be seen from the PD-TO solutions, the direction of the interior crack can significantly change the optimal topology. Besides,

the stiff material (in red) is mostly distributed over the regions with high strain energy for different crack orientations. Comparing the optimal results of these two methods indicates that the structures are generally very similar; however, there are some differences.The final topologies in [Banh and Lee(2018)] have multiple intermediate-phase areas where the optimization has not completely converged. This issue can be a result of the insufficient number of elements/design variables. Conversely, in the current method, we could achieve relatively better results in terms of convergence and connectivity of materials by using the same number of design variables. However, the topologies obtained from X-FEM method have slightly lower compliance relative to the PD-TO solutions. This is due to the fact that the compliance values of X-FEM and PD are evaluated based on two different theories, namely local and non-local. On the other hand, the surface correction factors are not considered in TO to reduce the computational cost. Additionally, the total displacement and strain energy density distributions obtained from PD analysis are illustrated in Figure 4.3. Also, the x and y components of the displacement are depicted in Figure 4.4.

It is notworthy that the X-FEM method does not provide an easy way to study the emergence and evolution of cracks. Namely, it requires some extra techniques to do so, in particular level-set methods, virtual crack closure, etc. Whereas, PD needs no special techniques to either predict damage initiation/growth in unspecified locations or control multiple damage sites and their complex interactions. Alternatively, it demands only one criterion for all of the above-mentioned processes, which is called the critical failure parameter and is based on energy release rate.

4.0.2 Example 1: Cantilever Beam

As shown in Figure 4.5, a cantilever beam is considered with a concentrated load $F = 1$ at the bottom of its free end. The design domain has a length to height ratio of 3:1. The ratio of Young's modulus for the two solid phases is 2:1. Also, the value of elastic modulus for the void phase is assumed to be 1×10^{-6} to avoid singularities. The volume constraints are 30% and 20% for the hard and soft materials, respectively, and these solid phases can occupy only 50% of the whole structure. The minimum filter radius is set to be 3. The discretization of the design domain is 90 particles along the length and 30 particles along the height. Also, to study the effect of an embedded crack on the optimal topology, an interior crack is modelled at the upper edge of the beam with the length of $l_c = 0.12H$ and at a distance of $t_c = 0.1166H$

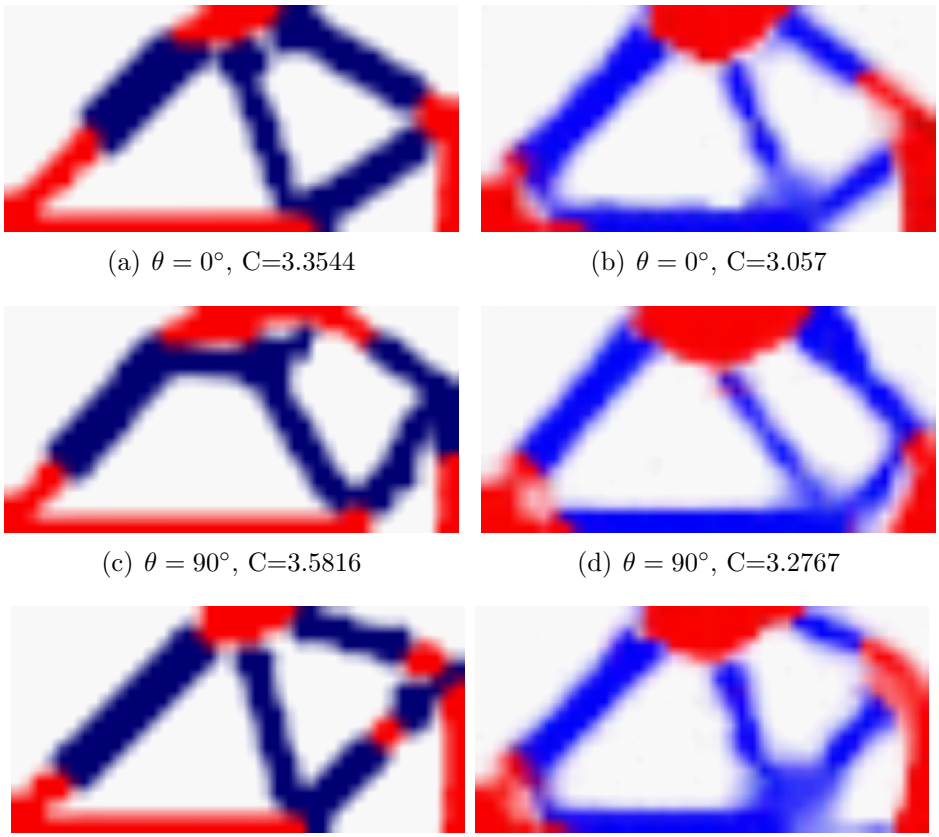

(a) $\theta = 0°$, C=3.3544 (b) $\theta = 0°$, C=3.057

(c) $\theta = 90°$, C=3.5816 (d) $\theta = 90°$, C=3.2767

(e) $\theta = 45°$, C=3.7674 (f) $\theta = 45°$, C=3.5143

Figure 4.2: Comparison of optimal solutions (left column: PD-TO results, right column: X-FEM results)

from the fixed end.

Figure 4.6 and Figure 4.7 display the optimal topologies of the cantilever beam, without and with initial crack, respectively. As can be seen from these figures, adding an initial crack into the structure can significantly affect the final topologies. Also, in the critical regions where the value of the strain energy is typically at its highest value (e.g, where the concentrated force is applied and the area close to the supports) we have the harder material (in red) to minimize the compliance as much as possible. Figure 4.8 and Figure 4.11 illustrates the strain energy density and total displacement distributions of the cantilever beam and the effect of the initial crack on them. Besides, the x and y components of the displacement can be found in Figure 4.9 and Figure 4.10.

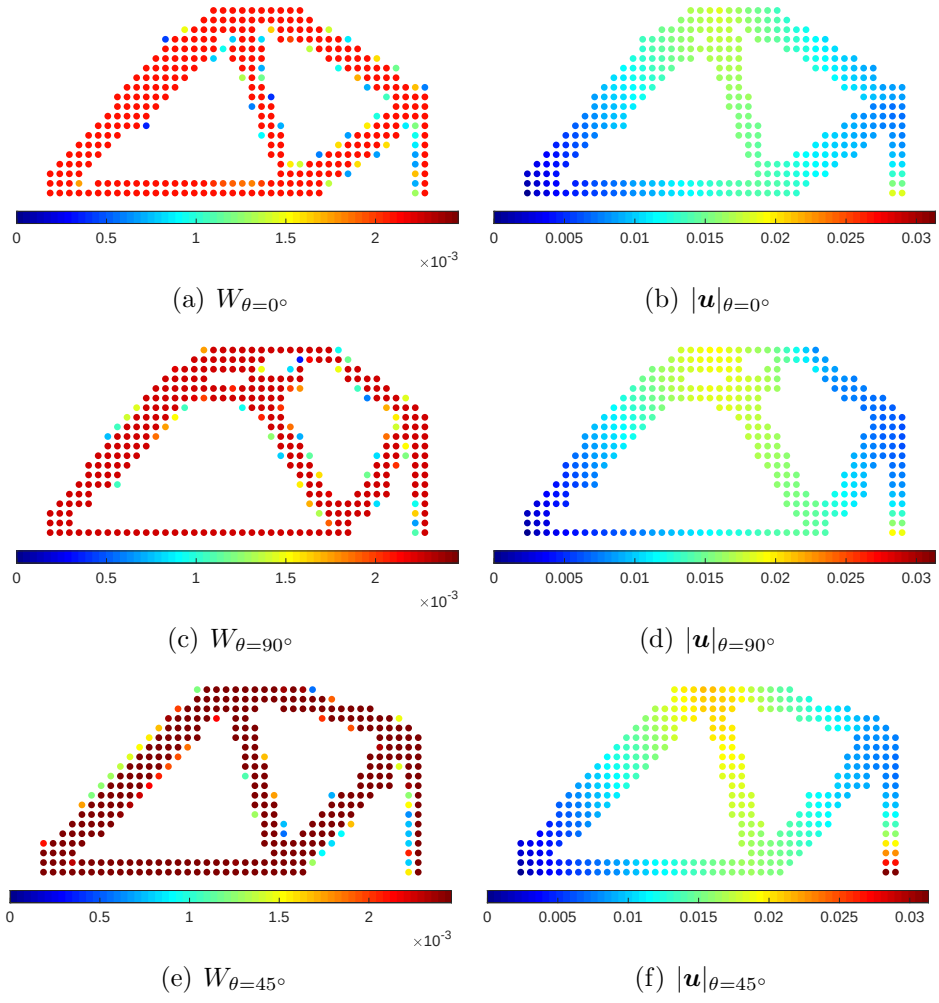

(a) $W_{\theta=0^\circ}$ (b) $|\boldsymbol{u}|_{\theta=0^\circ}$

(c) $W_{\theta=90^\circ}$ (d) $|\boldsymbol{u}|_{\theta=90^\circ}$

(e) $W_{\theta=45^\circ}$ (f) $|\boldsymbol{u}|_{\theta=45^\circ}$

Figure 4.3: Strain energy density (left column) and total displacement (right column) distribution of the horizontal, vertical, and inclined interior cracks

4.0.3 Example 2: L-Shape Structure

Figure 4.12 shows the design domain of the L-shape structure and its dimensions with $L = 1$. The beam is fully clamped at the top edge, and a downward concentrated force is applied to the structure with the magnitude of $F = 30$. The elastic modulus values are assumed to be the same as in Example 1. The corresponding volume constraints are 35% for the hard material, 20% for the soft material, and 45% for the void phase. Also, the minimum filer radius is equal to 3. A square-shape domain (including the L-shape design domain and the void area at the top right) is discretized by 60×60 material points. Moreover, the impact of an interior crack is studied by considering a horizontal crack of the length $l_c = 0.1L$ at the knee.

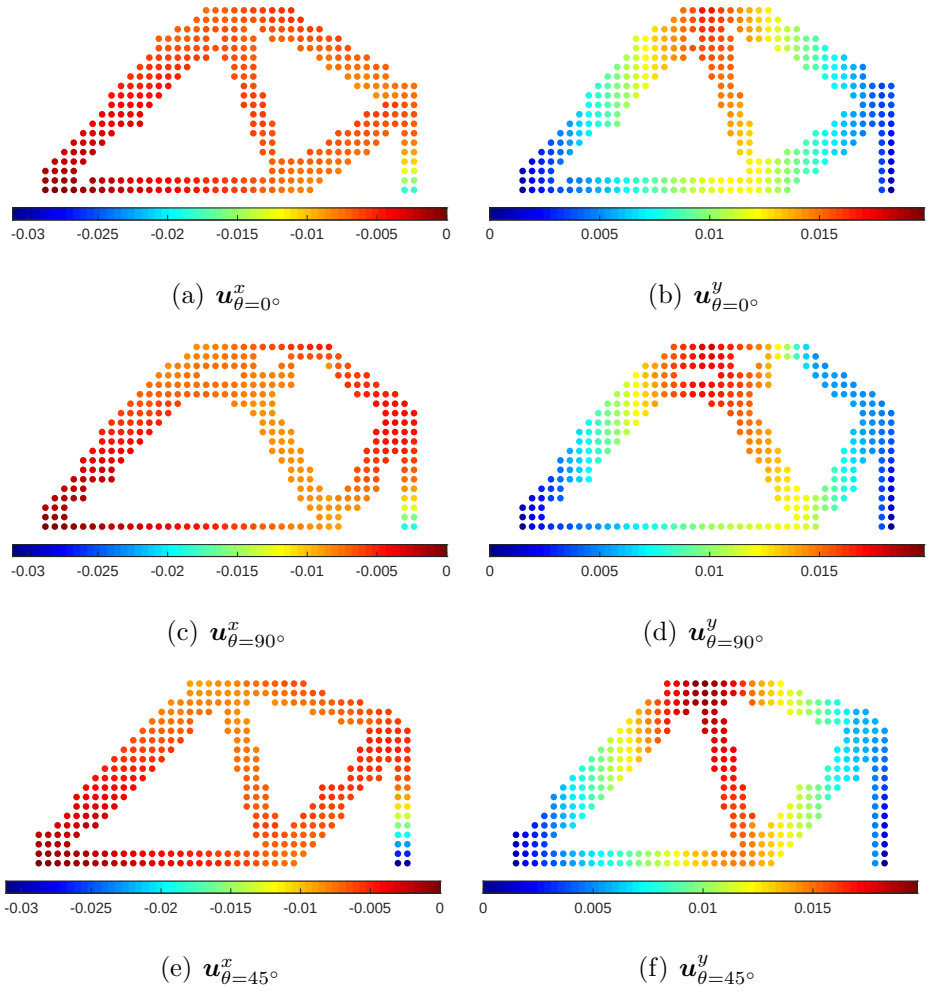

Figure 4.4: Displacement distribution of the horizontal, vertical, and inclined interior cracks in x (left column) and y directions (right column)

First, this example is solved without considering the crack, and the result is shown in Figure 4.13. Similar to the previous case, the critical areas close to the support and the location the concentrated force is applied are filled with the hard material to increase the stiffness of the structure. Next, the same example is solved, this time by taking into account an initial crack at the knee. Figure 4.14 illustrates that the distribution of the hard material (red color) has changed close to the crack tips to prevent crack propagation. Furthermore, Figure 4.15 and Figure 4.18 portray the distribution of the strain energy density and total displacement of the L-Shape structure without and with initially embedded cracks. The distribution of the displacement in x and y directions are given in Figure 4.16 and Figure 4.17.

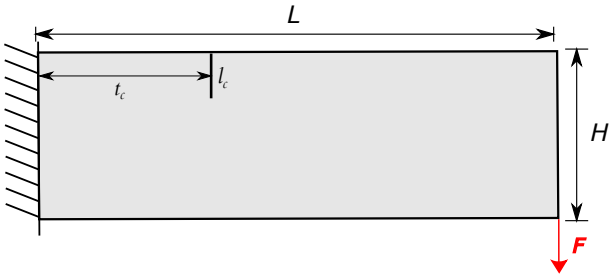

Figure 4.5: Design domain of the cantilever beam

Figure 4.6: Optimal design of the cantilever beam with no initial cracks

4.0.4 Example 3: Bridge with Uniform Pressure Load

In this example, a bridge, fully fixed at left and right edges is loaded by a uniform pressure $P = 1$. The length of the structure is two times greater than its width, and there are 80 and 40 particles along the length and the width of the bridge, respectively (Figure 4.19). The elastic modulus ratio of the hard to the soft material is 2:1. The value of Young's modulus of the void phase is the same as the previous cases. The volume constraints of hard and soft materials are 30% and 10%, respectively. The value of the minimum filter radius is assumed to be 3. A fixed layer of 6 particles in the vertical direction is considered; that is, the material points located in this area are fixed to have the hard material's Young's modulus, and it does not change throughout the optimization process. In addition, a crack of the length $l_c = 0.11H$ and at $t_c = 0.5L$ is modeled at the upper edge that passes through the fixed layer.

The optimal topologies of the bridge under uniform pressure are illustrated in Figure 4.20 for the structure without a crack and in Figure 4.21 for the cracked structure. By comparing these two figures, it can be stated that when there is an embedded crack, the value of the strain energy increases near the crack tips. Therefore, some extra amount of hard material is added to that region to reduce the magnitude of the strain energy (The small bump at the upper edge in Figure 4.21). Moreover, Figure 4.22 and Figure 4.25 show the strain energy density and total displacement distributions and the initial crack's affect on them. To provide more clarity, the x and

Figure 4.7: Optimal design of the cantilever beam with an initially embedded crack

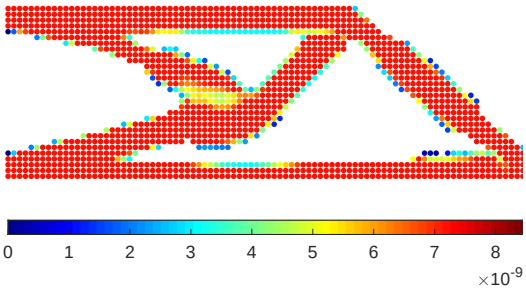

(a) No crack

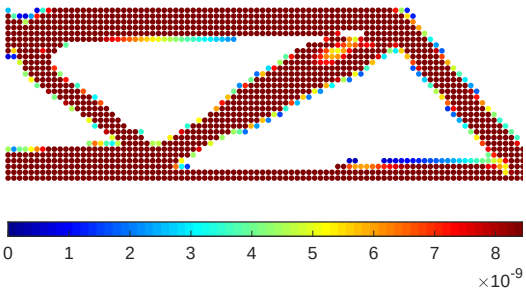

(b) Cracked

Figure 4.8: Strain energy density distribution of the cantilever beam

y components of the displacement are illustrated in Figure 4.23 and Figure 4.24.

4.0.5 Example 4: Bridge

The effect of the number of phases on the optimal topology is studied in this example. Figure 4.26 shows the design domain of a bridge. A concentrated load $F = 1$ is applied at the middle of the bottom edge. The left bottom corner is fixed, and the right bottom corner is simply supported. Moreover, two vertical cracks are placed at the bottom edge of the bridge at a horizontal distance of $t_c = 0.1L$ from the point where the force is applied. The length of the cracks is $l_c = 0.11H$. The ratio of the length to the height of the structure and the minimum filter radius value are the

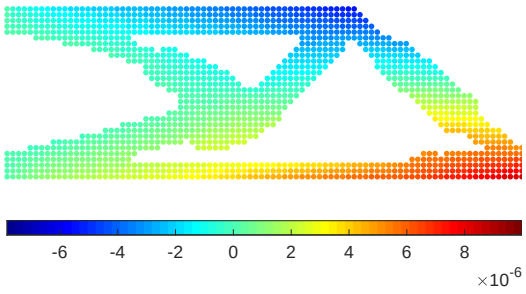

(a) No crack

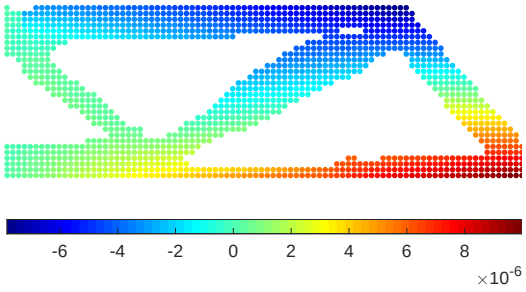

(b) Cracked

Figure 4.9: Displacement distribution of the cantilever beam in x-direction

same as Example 3. The values of the elastic moduli and the volume constraints of the three-phase and four-phase cases are summarized in Table 4.1. To decrease the computational cost, the symmetry of the structure and the applied loads is taken into account. Therefore, the design domain is discretized into 96×96 particles, distributed evenly over the domain and the target total volume constraint is chosen to be 60%.

	Number of materials	
Material properties	Three (red, blue, white)	Four (red, blue, green, white)
Young's modulus	$E_r = 2, E_b = 1, E_w = 1 \times 10^{-9}$	$E_r = 2, E_b = 1, E_g = 0.1, E_w = 1 \times 10^{-9}$
Volume fraction	$\omega_r = 35\%, \omega_b = 25\%, \omega_w = 40\%$	$\omega_r = 25\%, \omega_b = 20\%, \omega_g = 15\%, \omega_w = 40\%$

Table 4.1: Material properties of each material

The optimal solutions to the bridge problem with no cracks are shown in Figure 4.27 and Figure 4.28 for three and four material cases, respectively. It can be seen that the topologies are different, which implies the effect of the number of materials on the final topology. Furthermore, the cracked bridge case is solved to study the influence of cracks. Figure 4.29 illustrates the final topology of the cracked bridge using two solid materials. The result shows that the lower link in Figure 4.27 is removed so that

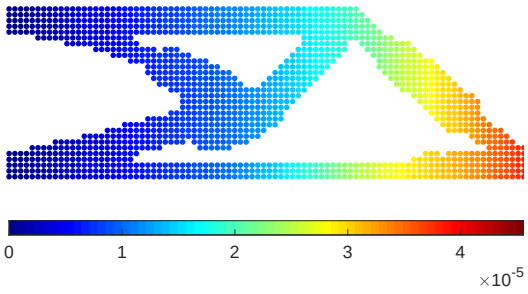

(a) No crack

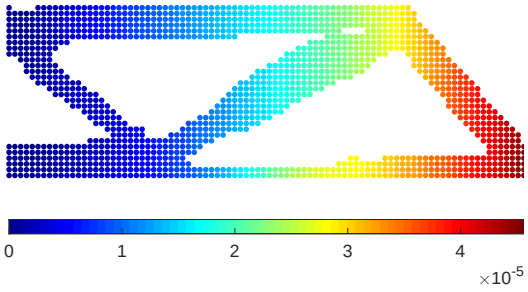

(b) Cracked

Figure 4.10: Displacement distribution of the cantilever beam in y-direction

the cracks are located in the void area. Consequently, the algorithm has prevented a rise in the strain energy of the structure. The solution of the cracked bridge using three solid materials is displayed in Figure 4.30. The same feature can be seen in this topology where the lower link is deleted compared to Figure 4.28. Moreover, Figure 4.31, Figure 4.34, Figure 4.35, and Figure 4.38 demonstrate the distribution of the strain energy and total displacement over the three and four material structures, respectively. Besides, the distribution of displacement in x and y directions are depicted in Figure 4.32 and Figure 4.33 for the three-material structure and in Figure 4.36 and Figure 4.37 for the four-material structure.

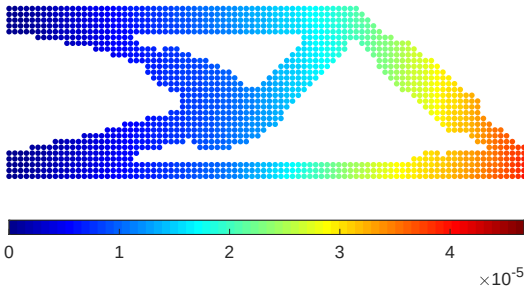

(a) No crack

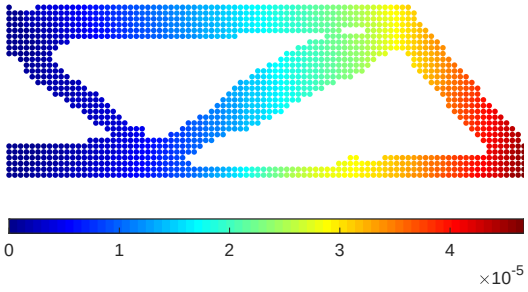

(b) Cracked

Figure 4.11: Total displacement distribution of the cantilever beam

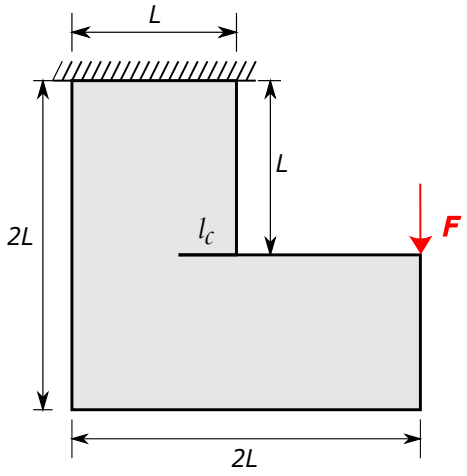

Figure 4.12: Design domain of the L-Shape structure

Figure 4.13: Optimal topology of the L-shape beam with no cracks

Figure 4.14: Optimal topology of the L-shape beam with an embedded crack at the knee

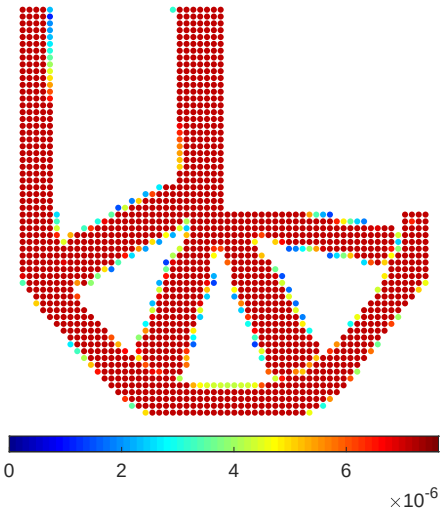

(a) No crack

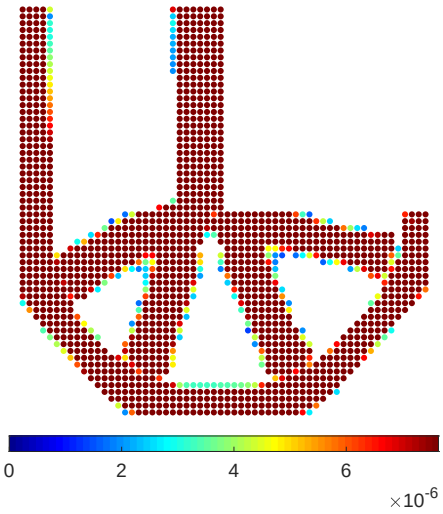

(b) Cracked

Figure 4.15: Strain energy density distribution of the L-Shape structure

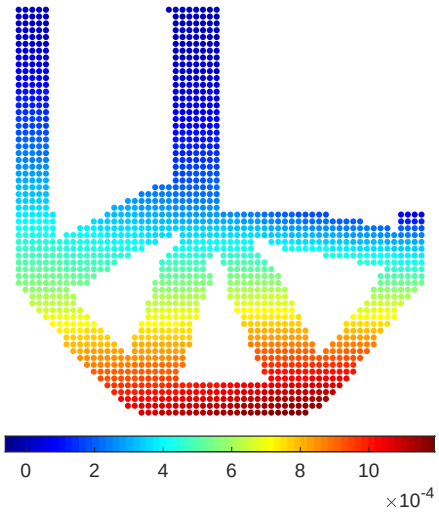

(a) No crack

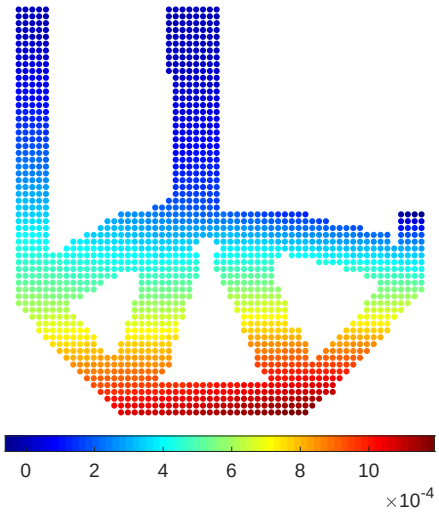

(b) Cracked

Figure 4.16: Displacement distribution of the L-Shape structure in x-direction

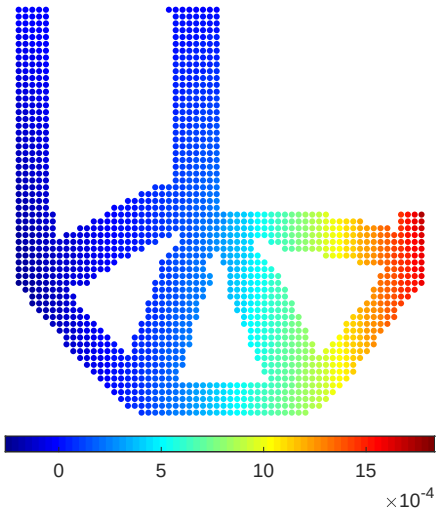

(a) No crack

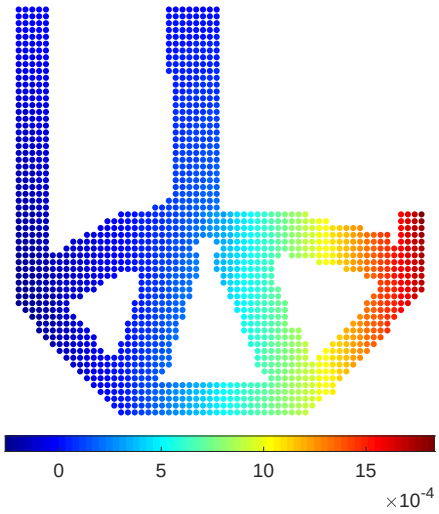

(b) Cracked

Figure 4.17: Displacement distribution of the L-Shape structure in y-direction

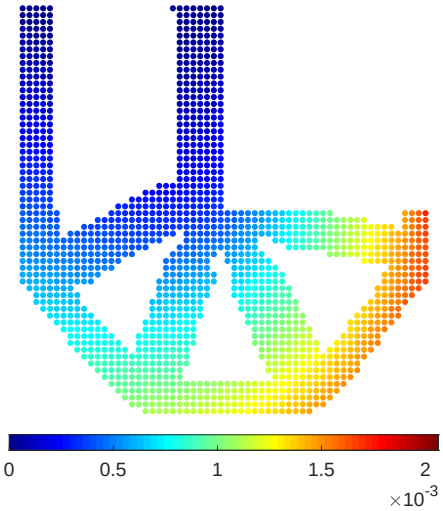

(a) No crack

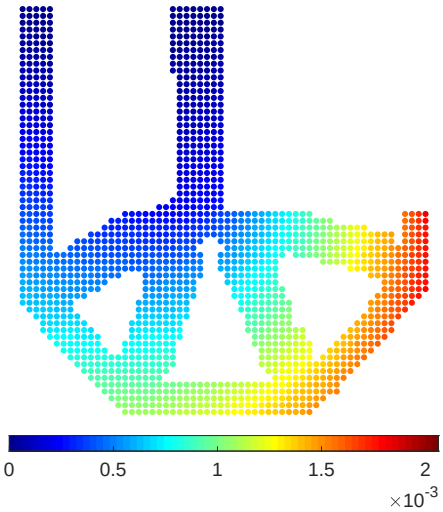

(b) Cracked

Figure 4.18: Total displacement distribution of the L-Shape structure

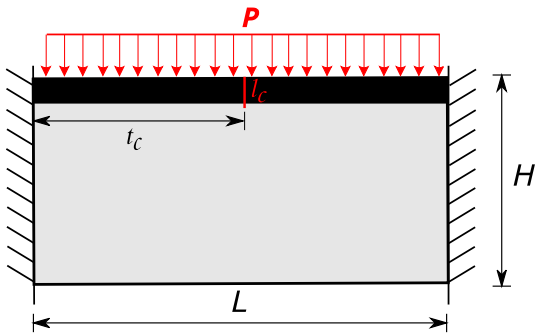

Figure 4.19: Design domain of the bridge with uniform pressure load

Figure 4.20: Optimal topology of the bridge under uniform pressure without initial crack

Figure 4.21: Optimal topology of the bridge under uniform pressure with an initially embedded crack

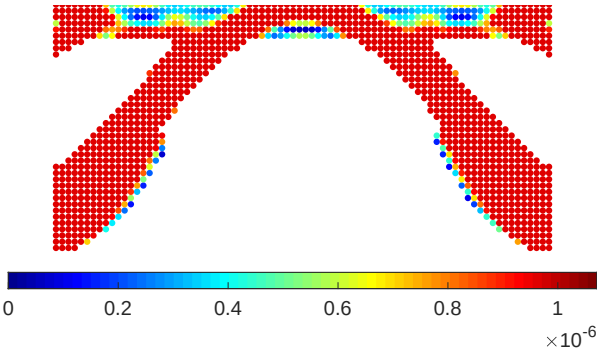

(a) No crack

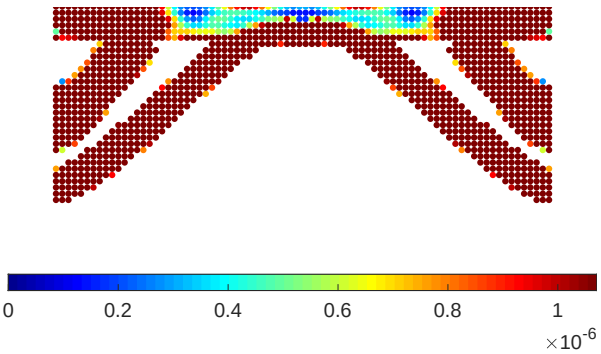

(b) Cracked

Figure 4.22: Strain energy density distribution of the bridge under uniform pressure

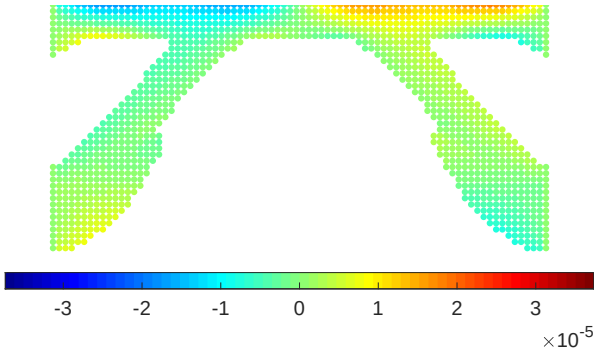

(a) No crack

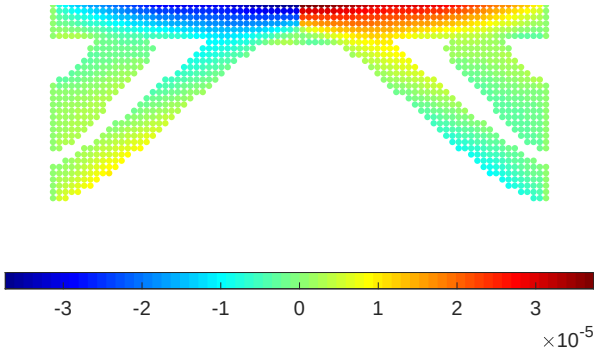

(b) Cracked

Figure 4.23: Displacement distribution of the bridge under uniform pressure in x-direction

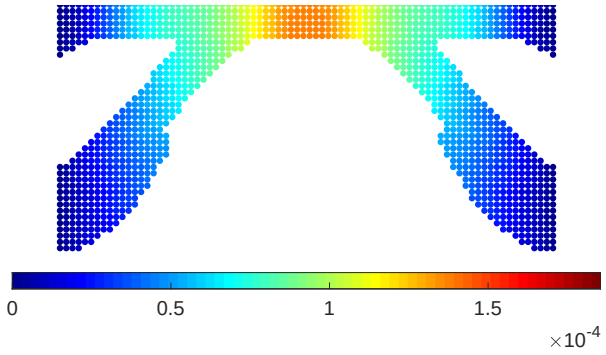

(a) No crack

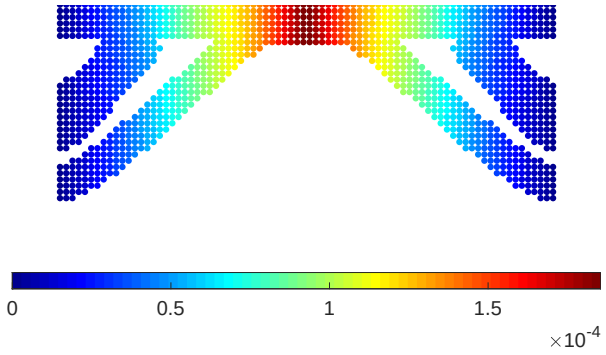

(b) Cracked

Figure 4.24: Displacement distribution of the bridge under uniform pressure in y-direction

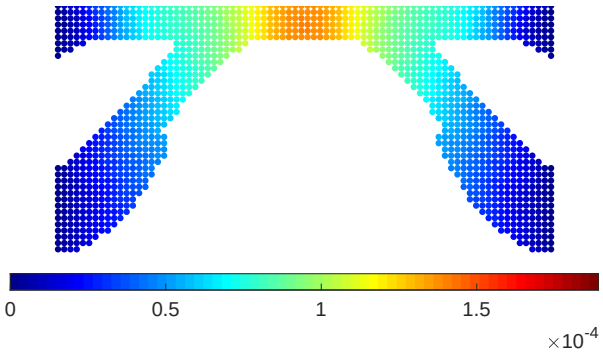

(a) No crack

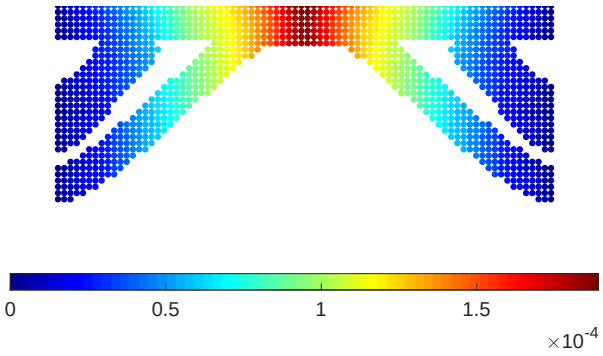

(b) Cracked

Figure 4.25: Total displacement distribution of the bridge under uniform pressure

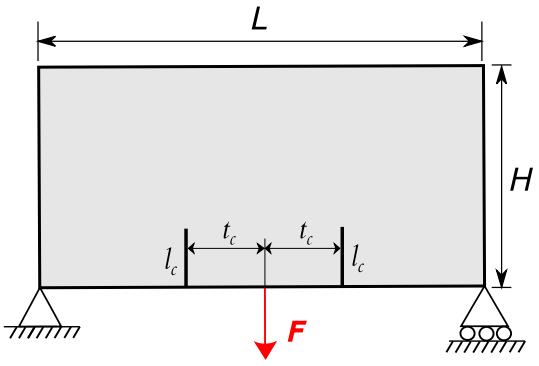

Figure 4.26: Design domain of the bridge with two interior cracks

Figure 4.27: Optimal result of the three-material bridge structure

Figure 4.28: Optimal result of the four-material bridge structure

Figure 4.29: Optimal result of the three-material cracked bridge structure

Figure 4.30: Optimal result of the four-material cracked bridge structure

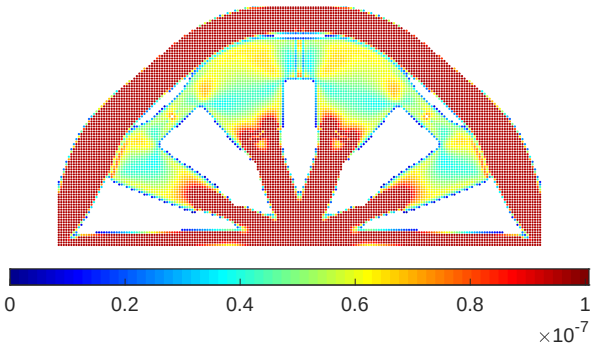

(a) No crack

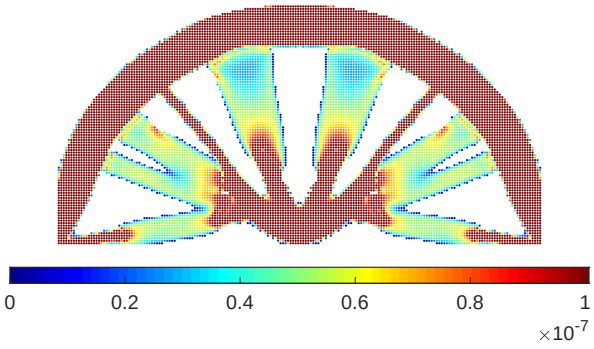

(b) Cracked

Figure 4.31: Strain energy density distribution of the three-material bridge

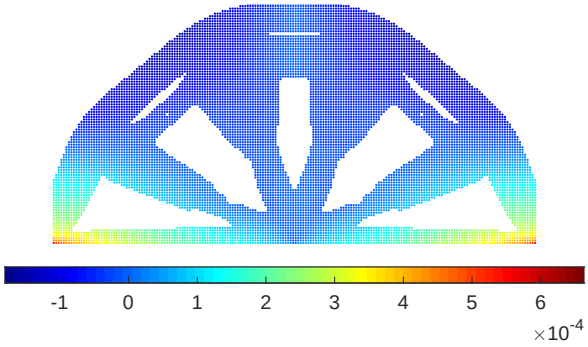

(a) No crack

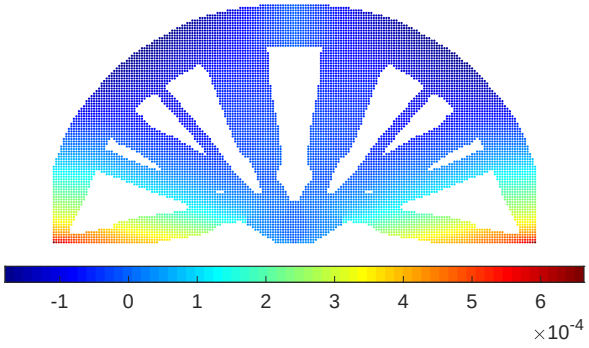

(b) Cracked

Figure 4.32: Displacement distribution of the three-material bridge in x-direction

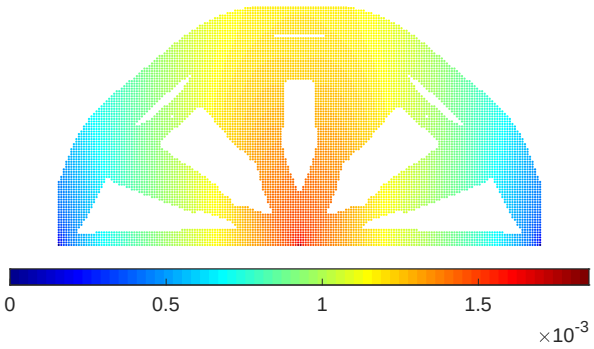

(a) No crack

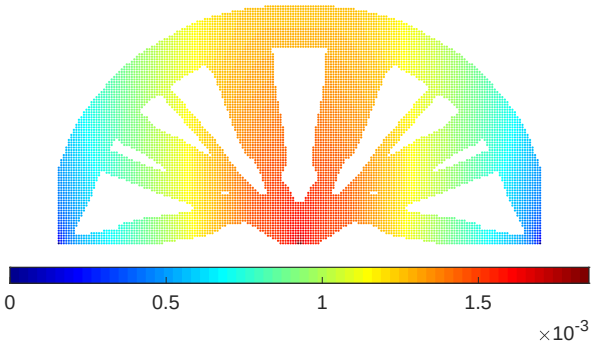

(b) Cracked

Figure 4.33: Displacement distribution of the three-material bridge in y-direction

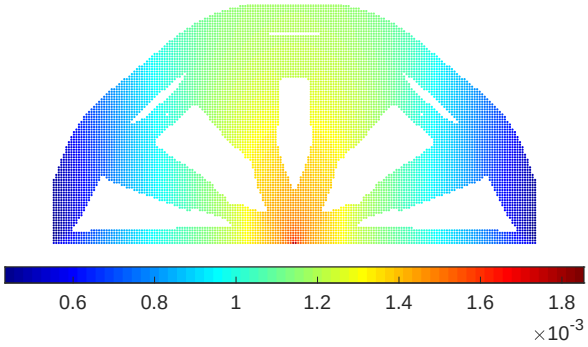

(a) No crack

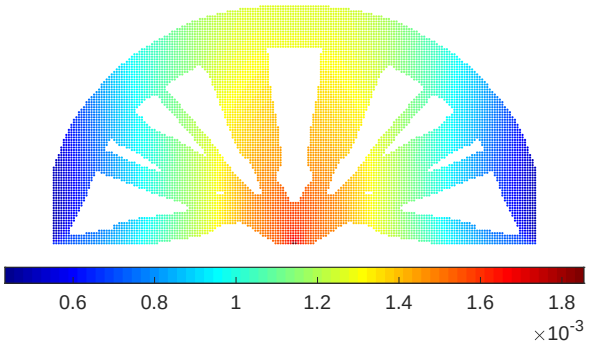

(b) Cracked

Figure 4.34: Total displacement distribution of the three-material bridge

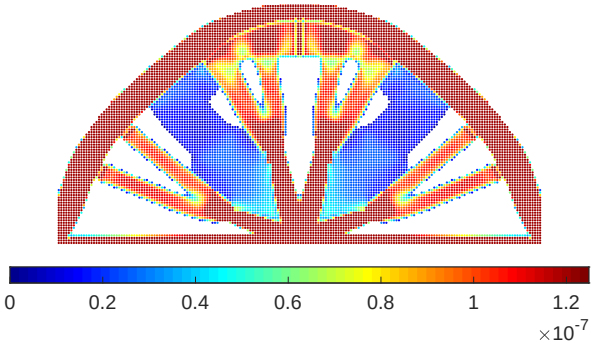

(a) No crack

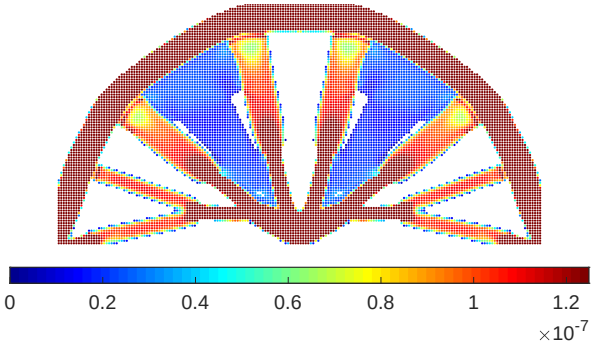

(b) Cracked

Figure 4.35: Strain energy density distribution of the four-material bridge

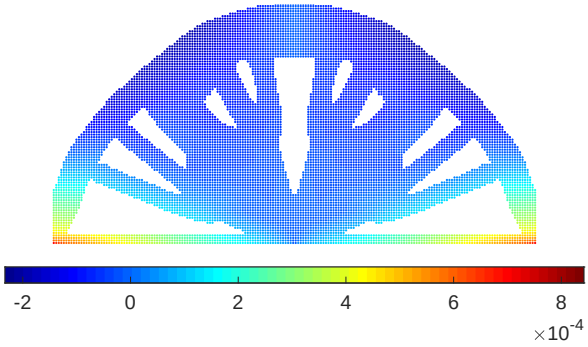

(a) No crack

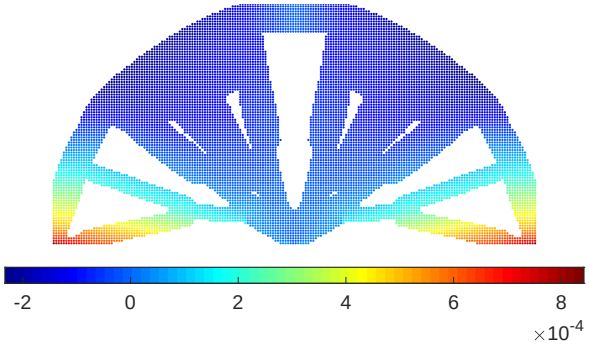

(b) Cracked

Figure 4.36: Displacement distribution of the four-material bridge in x-direction

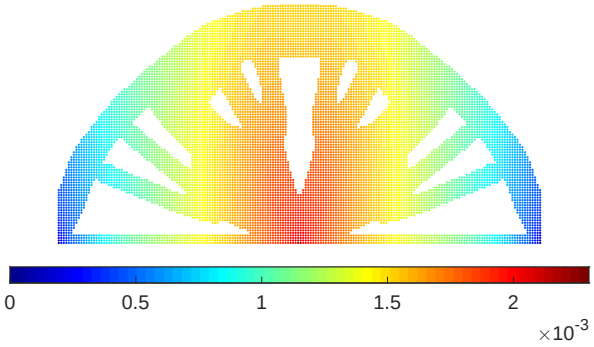

(a) No crack

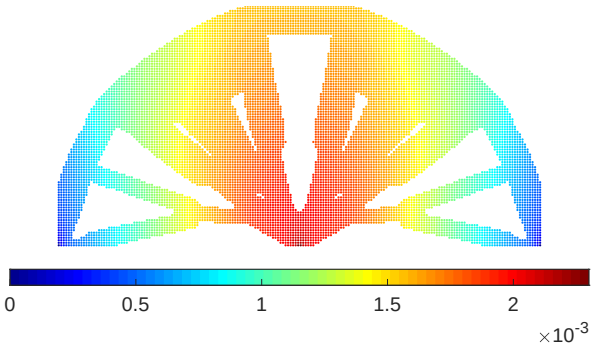

(b) Cracked

Figure 4.37: Displacement distribution of the four-material bridge in y-direction

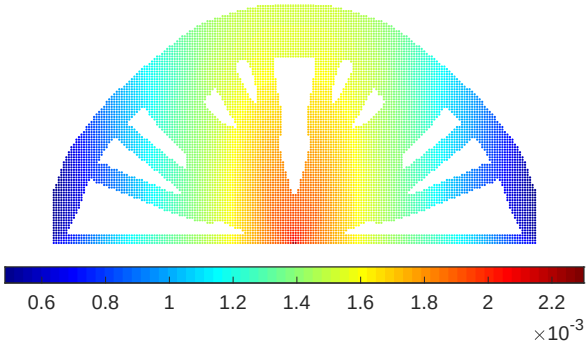

(a) No crack

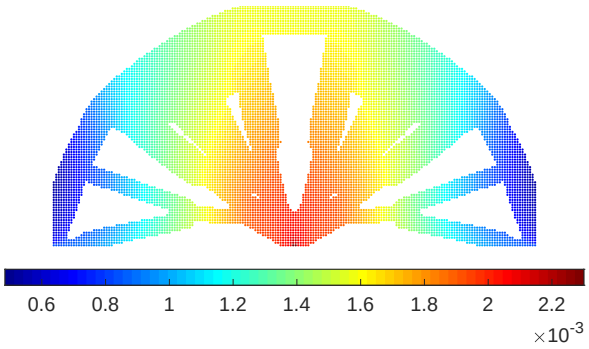

(b) Cracked

Figure 4.38: Total displacement distribution of the four-material bridge

Chapter 5

Conclusions and future work

The alternating active-phase algorithm is combined with the Peridynamics theory to solve density-based multi-material topology optimization problems. In this work, the direct solution method is used to solve the PD equations. As such, the computational cost of the proposed method is of the same order as mesh-based TO approaches.

First, the validity of the proposed method is investigated by comparing the results of three different cases against a work done by [Banh and Lee(2018)], where the same alternating active phase algorithm was used with the X-FEM approach. The results show good compatibility with their topologies while achieving relatively higher convergence. Note that mesh-based methods cannot handle crack modelling in a straightforward manner, and require complex algorithms to do so. Conversely, Peridynamics does not need any special treatments to solve problems involving moving boundary problems, large deformations, and damage presence since there is no necessity to maintain mesh connectivity. Next, the robustness of this method was studied through four examples by taking into account the impact of initial cracks on the optimal topologies.

The results show that initial cracks can notably influence the final design of the multi-material structures. In general, the PD-based topology optimization method adds/removes material points such that damaged regions are preferentially populated with material points to hinder crack propagation during/after optimization.

The usage of bond-based Peridynamics restricts the choice of materials since it imposes a constraint to the value of Poisson's ratio. As such, state-based formulation can be used for future work to remove this limit. Moreover, the alternating active-phase algorithm is a monotonic optimization solver; therefore, it cannot be used for non-monotonic optimization cases, such as problems involving design-dependent

loads. Hence, other non-monotonic optimization solvers can be utilized in further studies. Additionally, the present multi-material topology optimization approach can be extended to three-dimensional structures.

The focus of the current work is on topology optimization problems with volume constraints. Although, in recent years, some researchers have studied total mass constraint [Gao and Zhang(2011), Gao et al.(2016)Gao, Xu, and Zhang, Zuo and Saitou(2017), Yang and Li(2018)], which can be practical, especially from an engineering point of view. Considering the capabilities of the optimality criteria (OC) method, it is not straightforward to introduce mass constraints to the problem; however, this problem would be an interesting topic for future work in multi-material TO.

Appendix A

Balance of linear and angular momentum

Since for any material point $\boldsymbol{x}' \notin H$, $\boldsymbol{t}(\boldsymbol{x}' - \boldsymbol{x}, \boldsymbol{u}' - \boldsymbol{u}, t) = \boldsymbol{t}(\boldsymbol{x} - \boldsymbol{x}', \boldsymbol{u} - \boldsymbol{u}', t) = 0$, then the balance of momentum equations can include all of the material points in volume V by changing the limits of the integrals. Therefore, the balance of linear momentum, $\dot{\boldsymbol{M}} = \boldsymbol{F}$, and the balance of angular momentum, $\dot{\boldsymbol{H}}_o = \boldsymbol{\Pi}_{\boldsymbol{o}}$, lead to:

$$\begin{aligned}\int_V \rho(\boldsymbol{x})\ddot{\boldsymbol{u}}(\boldsymbol{x},t)dV = \int_V \boldsymbol{b}(\boldsymbol{x},t)dV + \int_V\int_V \boldsymbol{t}(\boldsymbol{x}' - \boldsymbol{x}, \boldsymbol{u}' - \boldsymbol{u}, t)dV'dV \\ - \int_V\int_V \boldsymbol{t}(\boldsymbol{x} - \boldsymbol{x}', \boldsymbol{u} - \boldsymbol{u}', t)dV'dV\end{aligned} \tag{A.1}$$

$$\begin{aligned}\int_V \boldsymbol{y}(\boldsymbol{x},t) \times \rho(\boldsymbol{x})\ddot{\boldsymbol{u}}(\boldsymbol{x},t)dV = \int_V \boldsymbol{y}(\boldsymbol{x},t) \times \boldsymbol{b}(\boldsymbol{x},t)dV + \int_V\int_V \boldsymbol{y}(\boldsymbol{x},t)\times \\ \boldsymbol{t}(\boldsymbol{x}' - \boldsymbol{x}, \boldsymbol{u}' - \boldsymbol{u}, t)dV'dV - \int_V\int_V \boldsymbol{y}(\boldsymbol{x},t) \times \boldsymbol{t}(\boldsymbol{x} - \boldsymbol{x}', \boldsymbol{u} - \boldsymbol{u}', t)dV'dV\end{aligned} \tag{A.2}$$

By exchanging the parameters $\boldsymbol{x}$ and $\boldsymbol{x}'$ one can conclude:

$$\int_V\int_V \boldsymbol{t}(\boldsymbol{x}' - \boldsymbol{x}, \boldsymbol{u}' - \boldsymbol{u}, t)dV'dV = \int_V\int_V \boldsymbol{t}(\boldsymbol{x} - \boldsymbol{x}', \boldsymbol{u} - \boldsymbol{u}', t)dV'dV \tag{A.3}$$

$$\int_V\int_V \boldsymbol{y}(\boldsymbol{x},t) \times \boldsymbol{t}(\boldsymbol{x}' - \boldsymbol{x}, \boldsymbol{u}' - \boldsymbol{u}, t)dV'dV = \int_V\int_V \boldsymbol{y}(\boldsymbol{x},t) \times \boldsymbol{t}(\boldsymbol{x} - \boldsymbol{x}', \boldsymbol{u} - \boldsymbol{u}', t)dV'dV \tag{A.4}$$

Bibliography

[AlKhateab et al.(2020)AlKhateab, Tabrizi, Zanjani, Rahimi, Poudeh, Kefal, and Yildiz] Baidaa AlKhateab, Isa Emami Tabrizi, Jamal Seyyed Monfared Zanjani, Mohammad Naqib Rahimi, Leila Haghighi Poudeh, Adnan Kefal, and Mehmet Yildiz. Damage mechanisms in CFRP/HNT laminates under flexural and in-plane shear loadings using experimental and numerical methods. *Composites Part A: Applied Science and Manufacturing*, 136:105962, sep 2020. ISSN 1359835X. doi: 10.1016/j.compositesa.2020.105962.

[Allaire and Jouve(2005)] Grégoire Allaire and François Jouve. A level-set method for vibration and multiple loads structural optimization. *Computer Methods in Applied Mechanics and Engineering*, 194(30-33 SPEC. ISS.):3269–3290, aug 2005. ISSN 00457825. doi: 10.1016/j.cma.2004.12.018.

[Allaire and Jouve(2008)] Grégoire Allaire and François Jouve. Minimum stress optimal design with the level set method. *Engineering Analysis with Boundary Elements*, 32(11):909–918, nov 2008. ISSN 09557997. doi: 10.1016/j.enganabound.2007.05.007.

[Allaire et al.(2004)Allaire, Jouve, and Toader] Grégoire Allaire, François Jouve, and Anca Maria Toader. Structural optimization using sensitivity analysis and a level-set method. *Journal of Computational Physics*, 194(1):363–393, feb 2004. ISSN 00219991. doi: 10.1016/j.jcp.2003.09.032.

[Allen and Cahn(1979)] Samuel M. Allen and John W. Cahn. A microscopic theory for antiphase boundary motion and its application to antiphase domain coarsening. *Acta Metallurgica*, 27(6):1085–1095, jun 1979. ISSN 00016160. doi: 10.1016/0001-6160(79)90196-2.

[Atluri and Zhu(1998)] S. N. Atluri and T. Zhu. A new Meshless Local Petrov-Galerkin (MLPG) approach in computational mechanics. *Computational Mechanics*, 22(2): 117–127, 1998. ISSN 01787675. doi: 10.1007/s004660050346.

[Banh and Lee(2018)] Thanh T. Banh and Dongkyu Lee. Multi-material topology optimization design for continuum structures with crack patterns. *Composite Structures*, 186:193–209, feb 2018. ISSN 02638223. doi: 10.1016/j.compstruct.2017.11.088.

[Barenblatt(1959)] G. I. Barenblatt. The formation of equilibrium cracks during brittle fracture. General ideas and hypotheses. Axially-symmetric cracks. *Journal of Applied Mathematics and Mechanics*, 23(3):622–636, jan 1959. ISSN 00218928. doi: 10.1016/0021-8928(59)90157-1.

[Basoglu et al.(2019)Basoglu, Zerin, Kefal, and Oterkus] Muhammed Fatih Basoglu, Zihni Zerin, Adnan Kefal, and Erkan Oterkus. A computational model of peridynamic theory for deflecting behavior of crack propagation with micro-cracks. *Computational Materials Science*, 162:33–46, may 2019. ISSN 09270256. doi: 10.1016/j.commatsci.2019.02.032.

[Belytschko et al.(1994)Belytschko, Lu, and Gu] T. Belytschko, Y. Y. Lu, and L. Gu. Element-free Galerkin methods. *International Journal for Numerical Methods in Engineering*, 37(2):229–256, jan 1994. ISSN 10970207. doi: 10.1002/nme.1620370205. URL `http://doi.wiley.com/10.1002/nme.1620370205`.

[Bendsøe(1989)] M. P. Bendsøe. Optimal shape design as a material distribution problem. *Structural Optimization*, 1(4):193–202, dec 1989. ISSN 09344373. doi: 10.1007/BF01650949.

[Bendsøe and Sigmund(1999)] M. P. Bendsøe and O. Sigmund. Material interpolation schemes in topology optimization. *Archive of Applied Mechanics*, 69(9-10):635–654, 1999. ISSN 09391533. doi: 10.1007/s004190050248.

[Bendsøe and Bendsøe(1995)] Martin P. Bendsøe and Martin P. Bendsøe. Introduction. In *Optimization of Structural Topology, Shape, and Material*, pages 1–4. Springer Berlin Heidelberg, 1995. doi: 10.1007/978-3-662-03115-5_1.

[Bendsøe and Kikuchi(1988)] Martin Philip Bendsøe and Noboru Kikuchi. Generating optimal topologies in structural design using a homogenization method. *Computer*

Methods in Applied Mechanics and Engineering, 71(2):197–224, nov 1988. ISSN 00457825. doi: 10.1016/0045-7825(88)90086-2.

[Blank et al.(2014)Blank, Farshbaf-Shaker, Garcke, Rupprecht, and Styles] Luise Blank, M. Hassan Farshbaf-Shaker, Harald Garcke, Christoph Rupprecht, and Vanessa Styles. Multi-material phase field approach to structural topology optimization. In *International Series of Numerical Mathematics*, volume 165, pages 231–246. Birkhäuser, Cham, 2014. doi: 10.1007/978-3-319-05083-6_15.

[Blasques(2014)] José Pedro Blasques. Multi-material topology optimization of laminated composite beams with eigenfrequency constraints. *Composite Structures*, 111(1):45–55, may 2014. ISSN 02638223. doi: 10.1016/j.compstruct.2013.12.021.

[Bourdin and Chambolle(2003)] Blaise Bourdin and Antonin Chambolle. Design-dependent loads in topology optimization. *ESAIM - Control, Optimisation and Calculus of Variations*, 9:247–273, jan 2003. ISSN 12623377. doi: 10.1051/cocv:2002070. URL `http://www.esaim-cocv.org/10.1051/cocv:2002070`.

[Bourdin and Chambolle(2006)] Blaise Bourdin and Antonin Chambolle. The phase-field method in optimal design. In *Solid Mechanics and its Applications*, volume 137, pages 207–215. Springer, Dordrecht, 2006. ISBN 1402047290. doi: 10.1007/1-4020-4752-5_21.

[Burger and Stainko(2006)] Martin Burger and Roman Stainko. Phase-field relaxation of topology optimization with local stress constraints. *SIAM Journal on Control and Optimization*, 45(4):1447–1466, oct 2006. ISSN 03630129. doi: 10.1137/05062723X.

[Cahn(1961)] John W. Cahn. On spinodal decomposition. *Acta Metallurgica*, 9(9):795–801, sep 1961. ISSN 00016160. doi: 10.1016/0001-6160(61)90182-1.

[Cahn and Hilliard(1958)] John W. Cahn and John E. Hilliard. Free energy of a nonuniform system. I. Interfacial free energy. *The Journal of Chemical Physics*, 28(2):258–267, feb 1958. ISSN 00219606. doi: 10.1063/1.1744102. URL `http://aip.scitation.org/doi/10.1063/1.1744102`.

[Cahn and Hilliard(1959)] John W. Cahn and John E. Hilliard. Free energy of a nonuniform system. III. Nucleation in a two-component incompressible fluid. *The*

Journal of Chemical Physics, 31(3):688–699, sep 1959. ISSN 00219606. doi: 10.1063/1.1730447. URL http://aip.scitation.org/doi/10.1063/1.1730447.

[Cheng et al.(2019)Cheng, Sui, Yin, Yuan, and Chu] Zhan Qi Cheng, Zhi Bo Sui, Hang Yin, Cheng Fang Yuan, and Liu Sheng Chu. Studies of dynamic fracture in functionally graded materials using peridynamic modeling with composite weighted bond. *Theoretical and Applied Fracture Mechanics*, 103:102242, oct 2019. ISSN 01678442. doi: 10.1016/j.tafmec.2019.102242.

[Cheng et al.(2015)Cheng, Zhang, Wang, and Bobaru] Zhanqi Cheng, Guanfeng Zhang, Yenan Wang, and Florin Bobaru. A peridynamic model for dynamic fracture in functionally graded materials. *Composite Structures*, 133:529–546, dec 2015. ISSN 02638223. doi: 10.1016/j.compstruct.2015.07.047.

[Cho and Kwak(2006)] Seonho Cho and Juho Kwak. Topology design optimization of geometrically non-linear structures using meshfree method. *Computer Methods in Applied Mechanics and Engineering*, 195(44-47):5909–5925, sep 2006. ISSN 00457825. doi: 10.1016/j.cma.2005.08.015.

[Cui et al.(2017)Cui, Chen, Zhou, and Wang] Mingtao Cui, Hongfang Chen, Jingling Zhou, and Fanglin Wang. A meshless method for multi-material topology optimization based on the alternating active-phase algorithm. *Engineering with Computers*, 33(4):871–884, 2017. ISSN 14355663. doi: 10.1007/s00366-017-0503-4.

[Dedè et al.(2012)Dedè, Borden, and Hughes] Luca Dedè, Micheal J. Borden, and Thomas J.R. Hughes. Isogeometric Analysis for Topology Optimization with a Phase Field Model. *Archives of Computational Methods in Engineering*, 19(3): 427–465, sep 2012. ISSN 11343060. doi: 10.1007/s11831-012-9075-z.

[Dugdale(1960)] D. S. Dugdale. Yielding of steel sheets containing slits. *Journal of the Mechanics and Physics of Solids*, 8(2):100–104, may 1960. ISSN 00225096. doi: 10.1016/0022-5096(60)90013-2.

[Eschenauer and Olhoff(2001)] Hans A. Eschenauer and Niels Olhoff. Topology optimization of continuum structures: A review. *Applied Mechanics Reviews*, 54(4):331–390, 2001. ISSN 00036900. doi: 10.1115/1.1388075. URL https://asmedigitalcollection.asme.org/appliedmechanicsreviews/article-pdf/54/4/331/5438226/331{_}1.pdf.

[Francfort and Marigo(1998)] G. A. Francfort and J. J. Marigo. Revisiting brittle fracture as an energy minimization problem. *Journal of the Mechanics and Physics of Solids*, 46(8):1319–1342, aug 1998. ISSN 00225096. doi: 10.1016/S0022-5096(98)00034-9.

[Gao and Zhang(2011)] Tong Gao and Weihong Zhang. A mass constraint formulation for structural topology optimization with multiphase materials. *International Journal for Numerical Methods in Engineering*, 88(8):774–796, nov 2011. ISSN 00295981. doi: 10.1002/nme.3197. URL `http://doi.wiley.com/10.1002/nme.3197`.

[Gao et al.(2016)Gao, Xu, and Zhang] Tong Gao, Pengli Xu, and Weihong Zhang. Topology optimization of thermo-elastic structures with multiple materials under mass constraint. *Computers and Structures*, 173:150–160, sep 2016. ISSN 00457949. doi: 10.1016/j.compstruc.2016.06.002.

[Griffits(1995)] A. A. Griffits. The phenomena of rupture and flow in solids. *Masinovedenie*, 221(1):9–14, jan 1995. ISSN 00254576. doi: 10.1098/rsta.1921.0006. URL `https://royalsocietypublishing.org/doi/10.1098/rsta.1921.0006`.

[He et al.(2014)He, Kang, and Wang] Qizhi He, Zhan Kang, and Yiqiang Wang. A topology optimization method for geometrically nonlinear structures with meshless analysis and independent density field interpolation. *Computational Mechanics*, 54(3):629–644, apr 2014. ISSN 01787675. doi: 10.1007/s00466-014-1011-7.

[Hu et al.(2012)Hu, Ha, and Bobaru] Wenke Hu, Youn Doh Ha, and Florin Bobaru. Peridynamic model for dynamic fracture in unidirectional fiber-reinforced composites. *Computer Methods in Applied Mechanics and Engineering*, 217-220:247–261, apr 2012. ISSN 00457825. doi: 10.1016/j.cma.2012.01.016.

[Hu and Madenci(2017)] Y. L. Hu and E. Madenci. Peridynamics for fatigue life and residual strength prediction of composite laminates. *Composite Structures*, 160:169–184, jan 2017. ISSN 02638223. doi: 10.1016/j.compstruct.2016.10.010.

[Huang et al.(2015)Huang, Lu, and Liu] Dan Huang, Guangda Lu, and Yiming Liu. Nonlocal peridynamic modeling and simulation on crack propagation in concrete structures. *Mathematical Problems in Engineering*, 2015, 2015. ISSN 15635147. doi: 10.1155/2015/858723. URL `http://dx.doi.org/10.1155/2015/858723`.

[Huang and Xie(2009)] X. Huang and Y. M. Xie. Bi-directional evolutionary topology optimization of continuum structures with one or multiple materials. *Computational Mechanics*, 43(3):393–401, jul 2009. ISSN 01787675. doi: 10.1007/s00466-008-0312-0.

[Hur et al.(2017)Hur, Kang, and Youn] Junyoung Hur, Pilseong Kang, and Sung Kie Youn. Topology optimization based on spline-based meshfree method using topological derivatives. *Journal of Mechanical Science and Technology*, 31(5): 2423–2431, may 2017. ISSN 1738494X. doi: 10.1007/s12206-017-0440-6.

[Javili et al.(2019)Javili, Morasata, Oterkus, and Oterkus] Ali Javili, Rico Morasata, Erkan Oterkus, and Selda Oterkus. Peridynamics review. *Mathematics and Mechanics of Solids*, 24(11):3714–3739, nov 2019. ISSN 17413028. doi: 10.1177/1081286518803411. URL `http://journals.sagepub.com/doi/10.1177/1081286518803411`.

[Juan et al.(2010)Juan, Shuyao, and Guangyao] Zheng Juan, Long Shuyao, and Li Guangyao. The topology optimization design for continuum structures based on the element free Galerkin method. *Engineering Analysis with Boundary Elements*, 34(7):666–672, jul 2010. ISSN 09557997. doi: 10.1016/j.enganabound.2010.03.001.

[Jung and Seok(2016)] Jeehyun Jung and Jongwon Seok. Fatigue crack growth analysis in layered heterogeneous material systems using peridynamic approach. *Composite Structures*, 152:403–407, sep 2016. ISSN 02638223. doi: 10.1016/j.compstruct.2016.05.077.

[Kang and Wang(2011)] Zhan Kang and Yiqiang Wang. Structural topology optimization based on non-local Shepard interpolation of density field. *Computer Methods in Applied Mechanics and Engineering*, 200(49-52):3515–3525, dec 2011. ISSN 00457825. doi: 10.1016/j.cma.2011.09.001.

[Kefal et al.(2019)Kefal, Sohouli, Oterkus, Yildiz, and Suleman] Adnan Kefal, Abdolrasoul Sohouli, Erkan Oterkus, Mehmet Yildiz, and Afzal Suleman. Topology optimization of cracked structures using peridynamics. *Continuum Mechanics and Thermodynamics*, 31(6):1645–1672, nov 2019. ISSN 14320959. doi: 10.1007/s00161-019-00830-x.

[Kilic and Madenci(2009)] Bahattin Kilic and Erdogan Madenci. Prediction of crack paths in a quenched glass plate by using peridynamic theory. *International*

Journal of Fracture, 156(2):165–177, may 2009. ISSN 03769429. doi: 10.1007/s10704-009-9355-2.

[le Hu et al.(2014)le Hu, Yu, and Wang] Yi le Hu, Yin Yu, and Hai Wang. Peridynamic analytical method for progressive damage in notched composite laminates. *Composite Structures*, 108(1):801–810, feb 2014. ISSN 02638223. doi: 10.1016/j.compstruct.2013.10.018.

[Liu et al.(1995)Liu, Jun, and Zhang] Wing Kam Liu, Sukky Jun, and Yi Fei Zhang. Reproducing kernel particle methods. *International Journal for Numerical Methods in Fluids*, 20(8-9):1081–1106, apr 1995. ISSN 10970363. doi: 10.1002/fld.1650200824. URL `http://doi.wiley.com/10.1002/fld.1650200824`.

[Luo and Kang(2013)] Yangjun Luo and Zhan Kang. Layout design of reinforced concrete structures using two-material topology optimization with Drucker-Prager yield constraints. *Structural and Multidisciplinary Optimization*, 47(1):95–110, jan 2013. ISSN 1615147X. doi: 10.1007/s00158-012-0809-1.

[Luo et al.(2012)Luo, Zhang, Gao, and Ma] Z. Luo, N. Zhang, W. Gao, and H. Ma. Structural shape and topology optimization using a meshless Galerkin level set method. *International Journal for Numerical Methods in Engineering*, 90 (3):369–389, apr 2012. ISSN 00295981. doi: 10.1002/nme.3325. URL `http://doi.wiley.com/10.1002/nme.3325`.

[Luo et al.(2009)Luo, Tong, Luo, Wei, and Wang] Zhen Luo, Liyong Tong, Junzhao Luo, Peng Wei, and Michael Yu Wang. Design of piezoelectric actuators using a multiphase level set method of piecewise constants. *Journal of Computational Physics*, 228(7):2643–2659, apr 2009. ISSN 10902716. doi: 10.1016/j.jcp.2008.12.019.

[Macek and Silling(2007)] Richard W. Macek and Stewart A. Silling. Peridynamics via finite element analysis. *Finite Elements in Analysis and Design*, 43(15):1169–1178, nov 2007. ISSN 0168874X. doi: 10.1016/j.finel.2007.08.012.

[Madenci and Oterkus(2014)] Erdogan Madenci and Erkan Oterkus. *Peridynamic theory and its applications*, volume 9781461484. Springer New York, jun 2014. ISBN 9781461484653. doi: 10.1007/978-1-4614-8465-3.

[Majdi and Reza(2020)] Behzad Majdi and Arash Reza. Multi-material topology optimization of compliant mechanisms via solid isotropic material with penalization approach and alternating active phase algorithm. *Proceedings of the Institution of Mechanical Engineers, Part C: Journal of Mechanical Engineering Science*, page 095440622090862, feb 2020. ISSN 20412983. doi: 10.1177/0954406220908627. URL http://journals.sagepub.com/doi/10.1177/0954406220908627.

[Monaghan(2012)] J.J. Monaghan. Smoothed Particle Hydrodynamics and Its Diverse Applications. *Annual Review of Fluid Mechanics*, 44(1):323–346, jan 2012. ISSN 0066-4189. doi: 10.1146/annurev-fluid-120710-101220. URL http://www.annualreviews.org/doi/10.1146/annurev-fluid-120710-101220.

[Mumford and Shah(1989)] David Mumford and Jayant Shah. Optimal approximations by piecewise smooth functions and associated variational problems. *Communications on Pure and Applied Mathematics*, 42(5):577–685, jul 1989. ISSN 10970312. doi: 10.1002/cpa.3160420503. URL http://doi.wiley.com/10.1002/cpa.3160420503.

[Osher and Sethian(1988)] Stanley Osher and James A. Sethian. Fronts propagating with curvature-dependent speed: Algorithms based on Hamilton-Jacobi formulations. *Journal of Computational Physics*, 79(1):12–49, 1988. ISSN 10902716. doi: 10.1016/0021-9991(88)90002-2.

[Ozdemir et al.(2020)Ozdemir, Kefal, Imachi, Tanaka, and Oterkus] M. Ozdemir, A. Kefal, M. Imachi, S. Tanaka, and E. Oterkus. Dynamic fracture analysis of functionally graded materials using ordinary state-based peridynamics. *Composite Structures*, 244:112296, jul 2020. ISSN 02638223. doi: 10.1016/j.compstruct.2020.112296.

[Querin et al.(2000a)Querin, Steven, and Xie] O. M. Querin, G. P. Steven, and Y. M. Xie. Evolutionary structural optimisation using an additive algorithm. *Finite elements in analysis and design*, 34(3-4):291–308, feb 2000a. ISSN 0168874X. doi: 10.1016/S0168-874X(99)00044-X.

[Querin et al.(2000b)Querin, Young, Steven, and Xie] O. M. Querin, V. Young, G. P. Steven, and Y. M. Xie. Computational efficiency and validation of bi-directional evolutionary structural optimization. *Computer Methods in Applied Mechan-*

ics and Engineering, 189(2):559–573, 2000b. ISSN 00457825. doi: 10.1016/S0045-7825(99)00309-6.

[Sethian and Wiegmann(2000)] J. A. Sethian and Andreas Wiegmann. Structural Boundary Design via Level Set and Immersed Interface Methods. *Journal of Computational Physics*, 163(2):489–528, sep 2000. ISSN 00219991. doi: 10.1006/jcph.2000.6581.

[Shobeiri(2015)] Vahid Shobeiri. The topology optimization design for cracked structures. *Engineering Analysis with Boundary Elements*, 58:26–38, 2015. ISSN 09557997. doi: 10.1016/j.enganabound.2015.03.002.

[Sigmund(2001)] O. Sigmund. Design of multiphysics actuators using topology optimization - Part II: Two-material structures. *Computer Methods in Applied Mechanics and Engineering*, 190(49-50):6605–6627, oct 2001. ISSN 00457825. doi: 10.1016/S0045-7825(01)00252-3.

[Silling(2000)] S. A. Silling. Reformulation of elasticity theory for discontinuities and long-range forces. *Journal of the Mechanics and Physics of Solids*, 48(1):175–209, jan 2000. ISSN 00225096. doi: 10.1016/S0022-5096(99)00029-0.

[Silling(2003)] S. A. Silling. Dynamic fracture modeling with a meshfree peridynamic code. In *Computational Fluid and Solid Mechanics 2003*, pages 641–644. Elsevier Inc., jun 2003. ISBN 9780080529479. doi: 10.1016/B978-008044046-0.50157-3.

[Silling(2010)] S. A. Silling. Linearized theory of peridynamic states. *Journal of Elasticity*, 99(1):85–111, mar 2010. ISSN 03743535. doi: 10.1007/s10659-009-9234-0.

[Silling and Askari(2005)] S. A. Silling and E. Askari. A meshfree method based on the peridynamic model of solid mechanics. In *Computers and Structures*, volume 83, pages 1526–1535. Pergamon, jun 2005. doi: 10.1016/j.compstruc.2004.11.026.

[Silling et al.(2007)Silling, Epton, Weckner, Xu, and Askari] S. A. Silling, M. Epton, O. Weckner, J. Xu, and E. Askari. Peridynamic states and constitutive modeling. *Journal of Elasticity*, 88(2):151–184, aug 2007. ISSN 03743535. doi: 10.1007/s10659-007-9125-1.

[Sohouli et al.(2020)Sohouli, Kefal, Abdelhamid, Yildiz, and Suleman] A. Sohouli, A. Kefal, A. Abdelhamid, M. Yildiz, and A. Suleman. Continuous density-based topology optimization of cracked structures using peridynamics.

Journal of Structural and Multidisciplinary Optimization, may 2020. doi: 10.1007/s00158-020-02608-1.

[Takezawa et al.(2010)Takezawa, Nishiwaki, and Kitamura] Akihiro Takezawa, Shinji Nishiwaki, and Mitsuru Kitamura. Shape and topology optimization based on the phase field method and sensitivity analysis. *Journal of Computational Physics*, 229(7):2697–2718, apr 2010. ISSN 10902716. doi: 10.1016/j.jcp.2009.12.017.

[Tavakoli and Mohseni(2014)] Rouhollah Tavakoli and Seyyed Mohammad Mohseni. Alternating active-phase algorithm for multimaterial topology optimization problems: A 115-line MATLAB implementation. *Structural and Multidisciplinary Optimization*, 49(4):621–642, oct 2014. ISSN 16151488. doi: 10.1007/s00158-013-0999-1.

[Underwood(1983)] P Underwood. *Computational Methods for Transient Analysis.* Computational methods in mechanics. North-Holland, 1983. ISBN 0444864792. URL `http://books.google.es/books?id=bZ9RAAAAMAAJ`.

[Vese and Chan(2002)] Luminita A. Vese and Tony F. Chan. A multiphase level set framework for image segmentation using the Mumford and Shah model. *International Journal of Computer Vision*, 50(3):271–293, dec 2002. ISSN 09205691. doi: 10.1023/A:1020874308076.

[Wang and Wang(2004)] Michael Yu Wang and Xiaoming Wang. "Color" level sets: A multi-phase method for structural topology optimization with multiple materials. *Computer Methods in Applied Mechanics and Engineering*, 193(6-8):469–496, feb 2004. ISSN 00457825. doi: 10.1016/j.cma.2003.10.008.

[Wang and Wang(2005)] Michael Yu Wang and Xiaoming Wang. A level-set based variational method for design and optimization of heterogeneous objects. *CAD Computer Aided Design*, 37(3):321–337, mar 2005. ISSN 00104485. doi: 10.1016/j.cad.2004.03.007.

[Wang and Zhou(2005)] Michael Yu Wang and Shiwei Zhou. Synthesis of shape and topology of multi-material structures with a phase-field method. In *Journal of Computer-Aided Materials Design*, volume 11, pages 117–138. Springer, jun 2005. doi: 10.1007/s10820-005-3169-y.

[Wang et al.(2003)Wang, Wang, and Guo] Michael Yu Wang, Xiaoming Wang, and Dongming Guo. A level set method for structural topology optimization. *Computer Methods in Applied Mechanics and Engineering*, 192(1-2):227–246, jan 2003. ISSN 00457825. doi: 10.1016/S0045-7825(02)00559-5.

[Wang et al.(2015)Wang, Luo, Kang, and Zhang] Yiqiang Wang, Zhen Luo, Zhan Kang, and Nong Zhang. A multi-material level set-based topology and shape optimization method. *Computer Methods in Applied Mechanics and Engineering*, 283:1570–1586, jan 2015. ISSN 00457825. doi: 10.1016/j.cma.2014.11.002.

[Xia et al.(2018)Xia, Da, and Yvonnet] Liang Xia, Daicong Da, and Julien Yvonnet. Topology optimization for maximizing the fracture resistance of quasi-brittle composites. *Computer Methods in Applied Mechanics and Engineering*, 332: 234–254, apr 2018. ISSN 00457825. doi: 10.1016/j.cma.2017.12.021.

[Xia and Wang(2008)] Qi Xia and Michael Yu Wang. Simultaneous optimization of the material properties and the topology of functionally graded structures. *CAD Computer Aided Design*, 40(6):660–675, jun 2008. ISSN 00104485. doi: 10.1016/j.cad.2008.01.014.

[Xie and Steven(1993)] Y. M. Xie and G. P. Steven. A simple evolutionary procedure for structural optimization. *Computers and Structures*, 49(5):885–896, dec 1993. ISSN 00457949. doi: 10.1016/0045-7949(93)90035-C.

[Yang et al.(1999)Yang, Xie, Steven, and Querin] X. Y. Yang, Y. M. Xie, G. P. Steven, and O. M. Querin. Bidirectional evolutionary method for stiffness optimization. *AIAA journal*, 37(11):1483–1488, may 1999. ISSN 00011452. doi: 10.2514/2.626.

[Yang and Li(2018)] Xingtong Yang and Ming Li. Discrete multi-material topology optimization under total mass constraint. *CAD Computer Aided Design*, 102: 182–192, sep 2018. ISSN 00104485. doi: 10.1016/j.cad.2018.04.023.

[Yin and Ananthasuresh(2001)] L. Yin and G. K. Ananthasuresh. Topology optimization of compliant mechanisms with multiple materials using a peak function material interpolation scheme. *Structural and Multidisciplinary Optimization*, 23 (1):49–62, dec 2001. ISSN 1615147X. doi: 10.1007/s00158-001-0165-z.

[Zhang et al.(2019)Zhang, Takezawa, and Kang] Xiaopeng Zhang, Akihiro Takezawa, and Zhan Kang. Robust topology optimization of vibrating structures considering random diffuse regions via a phase-field method. *Computer Methods in Applied Mechanics and Engineering*, 344:766–797, feb 2019. ISSN 00457825. doi: 10.1016/j.cma.2018.09.022.

[Zhang et al.(2001)Zhang, Liu, Song, and Lu] Xiong Zhang, Xiao Hu Liu, Kang Zu Song, and Ming Wan Lu. Least-squares collocation meshless method. *International Journal for Numerical Methods in Engineering*, 51(9):1089–1100, jul 2001. ISSN 00295981. doi: 10.1002/nme.200. URL `http://doi.wiley.com/10.1002/nme.200`.

[Zhang et al.(2018)Zhang, Ge, Zhang, and Zhao] Yaqing Zhang, Wenjie Ge, Yonghong Zhang, and Zhenfei Zhao. Topology optimization method with direct coupled finite element–element-free Galerkin method. *Advances in Engineering Software*, 115:217–229, 2018. ISSN 18735339. doi: 10.1016/j.advengsoft.2017.09.012.

[Zhao(2014)] Fei Zhao. Topology optimization with meshless density variable approximations and BESO method. *CAD Computer Aided Design*, 56:1–10, nov 2014. ISSN 00104485. doi: 10.1016/j.cad.2014.06.003.

[Zheng et al.(2009)Zheng, Long, Xiong, and Li] Juan Zheng, Shuyao Long, Yuanbo Xiong, and Guangyao Li. A finite volume meshless local petrov-galerkin method for topology optimization design of the continuum structures. Technical Report 1, 2009.

[Zhou and Rozvany(1991)] M. Zhou and G. I.N. Rozvany. The COC algorithm, Part II: Topological, geometrical and generalized shape optimization. *Computer Methods in Applied Mechanics and Engineering*, 89(1-3):309–336, 1991. ISSN 00457825. doi: 10.1016/0045-7825(91)90046-9.

[Zhou and Wang(2007)] Shiwei Zhou and Michael Yu Wang. Multimaterial structural topology optimization with a generalized Cahn-Hilliard model of multiphase transition. *Structural and Multidisciplinary Optimization*, 33(2):89–111, feb 2007. ISSN 1615147X. doi: 10.1007/s00158-006-0035-9.

[Zuo and Saitou(2017)] Wenjie Zuo and Kazuhiro Saitou. Multi-material topology optimization using ordered SIMP interpolation. *Structural and Multidisciplinary Optimization*, 55(2):477–491, feb 2017. ISSN 16151488. doi: 10.1007/s00158-016-1513-3.